Chemical Engineering Journal 481 (2024) 148384

Contents lists available at ScienceDirect

Chemical Engineering Journal

journal homepage: www.elsevier.com/locate/cej

Metal-organic frameworks' latent potential as High-Efficiency osmotic power generators in Thin-Film nanocomposite membranes

Sadegh Aghapour Aktij [a,b], Mostafa Dadashi Firouzjaei [b,c,*], Seyyed Arash Haddadi [d], Pooria Karami [a,b], Amirhossein Taghipour [b], Mehrasa Yassari [b], Asad Asad Asad [e], Mohsen Pilevar [c], Hesam Jafarian [c], Mohammad Arjmand [d], Mark Elliott [c], Ahmad Rahimpour [b,*], João B.P. Soares [a,*], Mohtada Sadrzadeh [b,*]

[a] Department of Chemical & Materials Engineering, 12-263 Donadeo Innovation Centre for Engineering, Group of Applied Macromolecular Engineering, University of Alberta, Edmonton, AB, T6G 1H9, Canada
[b] Department of Mechanical Engineering, 10-367 Donadeo Innovation Center for Engineering, Advanced Water Research Lab (AWRL), University of Alberta, Edmonton, AB, T6G 1H9, Canada
[c] Department of Civil, Environmental, and Construction Engineering, University of Alabama, Tuscaloosa, AL 35487, USA
[d] Nanomaterials and Polymer Nanocomposites Laboratory, School of Engineering, University of British Columbia, Kelowna, BC V1V 1V7, Canada
[e] Department of Mechanical Engineering, University of Alberta, Nanotechnology Research Centre, T6G 2M9, Canada

ARTICLE INFO

Keywords:
Metal-organic framework (MOF)
Thin-film nanocomposite (TFN) membranes
Pressure retarded osmosis (PRO)
Osmotic power generation
Power density

ABSTRACT

This study investigates enhanced osmotic power generation by incorporating metal–organic framework (MOF) nanorods into the thin-film nanocomposite (TFN) membranes for pressure retarded osmosis (PRO) applications. The spotlight is on an innovative membrane, NH_2-Ce-BTC-500, which is fabricated utilizing amine-functionalized MOFs (NH_2-Ce-BTC), showcasing the synergistic effects of structure and chemistry in optimizing membrane properties for power generation. The NH_2-Ce-BTC-500 membrane exhibits a remarkable increase in hydrophilicity, setting a new power density benchmark of 6.9 W/m^2. NH_2-Ce-BTC-500 outperforms Ce-BTC-500 and pristine TFC membranes by 15 % and 109.1 %, demonstrating the superior performance of amine-functionalized membranes. Furthermore, through physical and chemical characterizations, it is revealed that the MOF-based membranes exhibit increased surface roughness and porosity, indicating the formation of additional water pathways. This enhancement leads to a substantial increase in the water flux, reaching 31.0 LMH in PRO mode, which is a 106 % improvement compared to pristine TFC membranes. This remarkable increase in water flux directly translates to enhanced power generation capacity. In essence, the NH_2-Ce-BTC-500 membrane exhibits promising advancements in PRO performance, offering the potential to lower downstream energy consumption and increase power generation efficiency. This research opens up a new paradigm for developing next-generation osmotic power generation. This renewable and energy-efficient solution can address the global energy crisis by leveraging the potential of MOF nanorods in TFN membranes.

1. Introduction

The global demand for fresh water is expected to rise by 20–30 % by 2050, driven by an anticipated population increase of 9.8 billion and growing pressures from the industrial and agricultural sectors [1,2]. Concurrently, the need for electricity is projected to increase by 50 % by 2040 [3], partly due to the need to reduce greenhouse gas emissions, which have increased by about 1 % per year over the last decade [4,5]. In response, researchers are actively pursuing the development of novel renewable energy sources, which already account for 26.3 % of global power generation, and advanced desalination and wastewater treatment techniques. The desalination capacity reached 96 million m^3/day in 2019 [6]. Membrane processes that use osmotic pressure, specifically pressure-retarded osmosis (PRO), have emerged as promising and

* Corresponding authors at: Department of Mechanical Engineering, 10-367 Donadeo Innovation Center for Engineering, Advanced Water Research Lab (AWRL), University of Alberta, Edmonton, AB, T6G 1H9, Canada (M.D. Firouzjaei).
E-mail addresses: mdfirouzjaei@crimson.ua.edu (M. Dadashi Firouzjaei), arahimpo@ualberta.ca (A. Rahimpour), jsoares@ualberta.ca (J.B.P. Soares), sadrzade@ualberta.ca (M. Sadrzadeh).

https://doi.org/10.1016/j.cej.2023.148384
Received 12 September 2023; Received in revised form 10 December 2023; Accepted 26 December 2023
Available online 28 December 2023

sustainable strategies with improved water flux and energy consumption compared to traditional techniques [7].

PRO utilizes the osmotic pressure gradient to enable the passage of water molecules from a low salinity feed solution (such as river water, wastewater, or brackish water) to a high salinity draw solution (such as brine and seawater) through a semipermeable membrane. This process is complemented by applying an external hydraulic pressure on the draw solution [8–10]. While PRO has been studied for decades, the lack of efficient separation membranes with high water permeability and solute selectivity has impeded its advancement in surpassing existing water purification and power generation technologies [11]. Early commercial cellulose acetate membranes, for example, demonstrated limitations in PRO applications, primarily due to their low water flux and, subsequently, low power density (<1 W/m^2) [12]. To address these challenges, researchers have shifted their attention toward developing thin-film composite (TFC) membranes. These membranes exhibit enhanced solute selectivity and water permeability, positioning them as essential components in optimizing osmotic filtration processes [13,14].

Recent advancements in the development of osmotic membranes, notable for their remarkable transport and structural characteristics [15–17], have heightened expectations for fabricating high-efficiency PRO membranes with enhanced osmotic power generation. The current literature suggests that engineering the polyamide selective layer by integrating a functionalized nanoscale material layer holds promise for creating highly effective TFN membranes tailored for osmotic power generation [15–17]. In a study by Gonzales et al. [18], a hydrophobic porous polymer nanomaterial was chemically modified into a sulfonate-functionalized variant, PP-SO_3H, with hydrophilic characteristics using chlorosulfonic acid. Integration of 0.002 wt% PP-SO_3H into the polyamide layer significantly enhanced water flux to 46.3 LMH, a substantial improvement over the 31.4 LMH flux of the unmodified membrane, using deionized water and 1.0 M NaCl as the feed and draw streams, respectively. Power density also increased remarkably, reaching 14.6 W/m^2 at a 17 bar pressure difference, compared to the maximum 8.2 W/m^2 achieved by the unmodified membrane. In another study, Li et al. [19] enhanced TFC membranes for PRO by incorporating carbon quantum dots (CQDs) into the polyamide selective layers. This modification, involving original CQDs (O-CQD) and Na^+–functionalized CQDs (Na-CQD), improved hydrophilicity, increased surface area, and altered the polyamide layer's structure, resulting in a more open and thinner network. The most effective membrane, containing 1 wt% Na–CQD-9, demonstrated superior performance, exhibiting increased water flux from 44.52 to 53.54 LMH and about 20 % higher power density at 23 bar when tested with 1.0 M NaCl and deionized water as the feed solution. These studies highlight the potential of incorporating small quantities of functionalized nanomaterials into the polyamide layer, offering a promising avenue for advancing high-performance PRO membranes on a larger scale [15,18].

Conventional TFC PRO membranes often encounter challenges such as unfavorable reverse solute flux and fouling, leading to decreased desalination efficiency and power density [11]. As a result, optimizing water purification and power generation technologies requires the development of advanced TFC PRO membranes with superior water permeability coefficients [15]. Innovations in membrane technology are increasingly centered on integrating nanomaterials, a strategy that significantly improves the membrane porosity, permeability, and reactivity [15–17]. These nanomaterials, whether dispersed within or immobilized on the membrane support or its selective layer, lead to the formation of either mixed matrix membranes (MMMs) or TFN membranes [20,21]. This integration plays a crucial role in altering the membranes' morphology and other essential characteristics. Some of the nanomaterials in previous membrane development studies include metal oxides [20,22], silica [23], titania nanosheets [23], MXenes [24], carbon-based materials (graphene, carbon nanotube, carbon nanofibers) [25,26], and metal–organic frameworks (MOFs) [27–31].

MOFs are composed of organic ligands and metal ions that are connected to form one-, two-, or three-dimensional coordination networks [31–33]. The physicochemical properties of MOFs, such as pore size, hydrophilicity, and surface functionality, can be customized to improve their compatibility with the membrane [34–37]. For example, by selecting metal ions and organic linkers with appropriate functional groups, such as amine, carboxyl, or hydroxyl groups, researchers could establish strong intermolecular interactions, e.g., hydrogen bonding, between MOFs and polyamide chains [30,38]. These interactions can improve MOF dispersion within the polyamide layer, reducing aggregation and improving the overall structural integrity of the composite membrane [39]. Advanced composite membranes with enhanced separation performance and reduced fouling can be developed by strategically tailoring MOFs, leading to significant improvements in the efficiency of the PRO process for water purification and power generation technologies [26]. Ma et al. and Firouzjaei et al. incorporated zirconium (IV)-carboxylate MOF UiO-66 NPs and GO–Ag-MOF nanomaterials into polyamide layers by dispersing them in the organic and aqueous solutions during interfacial polymerization, respectively [26,40]. The inclusion of MOF nanomaterials in the membranes resulted in notable changes in the membrane structure and chemistry, thereby improving intrinsic separation properties due to molecular sieving and the highly hydrophilic nature of the nanoparticles. The water permeability of TFC membranes modified with Zr-MOFs and GO–Ag-MOFs increased by 52 % and 113 %, respectively, accompanied by enhanced selectivity. The modified membranes containing 0.1 wt% Zr-MOFs exhibited the highest water flux, with 27 LMH and 51.3 LMH in forward osmosis (FO) and PRO modes, respectively. Similarly, the modified membranes with 0.03 wt% GO-Ag-MOF showed the highest water permeability at 2.45 LMH bar^{-1}.

Despite the successful results reported in the literature regarding the fabrication of MOF-based TFN membranes, some challenges still hinder their full deployment [28,29,31,41]. These challenges include the complexity of MOF synthesis processes, the stability and longevity of MOFs under real-world operating conditions, and concerns about MOF release during long-term filtration and its potential environmental impacts. In this work, we aimed to overcome some of these challenges by incorporating properly functionalized cerium-trimesic acid (Ce-BTC) MOFs into the polyamide membrane's active layer for the first time, resulting in defect-free and highly stable nanocomposite membranes with improved power density and transport properties. Cerium is a chemical element known for its soft and biocompatible properties, which is found in many minerals, including monazite, bastnasite, and xenotime [42]. Cerium ions (Ce^{3+}) have exhibited properties of hard acids with an eco-friendly nature, non-toxic, and selective behavior [43]. Many environmental researchers have recently investigated the application of MOFs containing elements like cerium and lanthanum as effective adsorbents for toxic ion removal [42,44,45]. In addressing the formidable challenges within the realm of osmotic power generation, our study marks a significant advancement in TFN membrane technology. Our investigation takes a unique path by integrating MOF nanorods, specifically Ce-BTC and its amine-functionalized variant (NH_2-Ce-BTC), into the membrane structure. This innovative approach is not merely an incremental improvement but a significant leap forward in addressing several limitations of current PRO membrane technologies. To our knowledge, this study marks the first-ever use of cerium-based MOFs in the production of TFC membranes specifically designed for clean energy generation, desalination, and wastewater treatment. The integration of Ce-BTC and NH_2-Ce-BTC MOFs into TFN membranes is a groundbreaking development in membrane technology, offering promising solutions to enhance PRO process efficiency. Beyond its impact on membrane engineering, this innovative use of cerium-based MOFs highlights their vast potential in environmental applications, paving the way for sustainable water treatment and energy generation technologies.

To fabricate novel MOF-based TFN membranes in this study, Ce-BTC and amine-functionalized Ce-BTC (NH_2-Ce-BTC) were synthesized and

used to make Ce-BTC and NH_2-Ce-BTC TFN membranes. Comprehensive characterization confirmed the functionalization strategy's success and revealed information about the chemical and morphological properties of the synthesized MOFs. PRO experiments were used to assess the effects of MOF incorporation on the transport properties and power generation of TFN membranes, and the performance of the pristine TFC membrane was compared.

2. Materials and methods

2.1. Chemicals

All chemicals were used as received. Commercial polyethersulfone (PES) substrates with a pore size of 200 nm were supplied by Sterlitech Co. M−phenylene diamine (MPD, >99 %), trimesoyl chloride (TMC, 98 %), trimesic acid (>95 %), cerium nitrate ($Ce(NO_3)_3$, >99 %), and (3-aminopropyl)triethoxysilane (APTES, >98 %) were all obtained from Sigma-Aldrich. Sodium dodecyl sulfate (SDS), sodium chloride (NaCl), n-heptane, ethanol (>96 %), and triethylamine (TEA) were purchased from Fisher Scientific.

2.2. Preparation and characterization of Ce-BTC and NH_2-Ce-BTC MOFs

Ce-BTC MOFs were synthesized according to the method mentioned in [46]. For this purpose, 0.05 mol $Ce(NO_3)_3$ and 0.05 mol trimesic acid were dissolved separately in DI water (50 mL) and ethanol (50 mL), respectively. Then, two solutions were transferred to a 200 mL Erlenmeyer flask under stirring for 2 h at 90 °C. Next, the obtained Ce-BTC MOFs were centrifugated and washed several times with DI water/ethanol mixture (1:1 v/v) to remove all unreacted components and impurities.

To functionalize Ce-BTC MOFs with amine (–NH_2) groups and obtain NH_2-Ce-BTC MOFs, Ce-BTC MOFs were modified by APTES. In the first step, 1 g Ce-BTC MOFs were dispersed in 90 mL ethanol containing 1 mL of APTES. The prepared suspension remained under agitation for 36 h at 78 °C. Finally, the functionalized NH_2-Ce-BTC MOFs were filtered, washed three times with ethanol, and dried in an oven at 55 °C for 30 h.

SEM-EDX (Zeiss Leo 1530, Japan) was employed to study the morphology/chemical composition of synthesized Ce-BTC MOFs and NH_2-Ce-BTC MOFs. The chemical bonds and valence states of O, Ce, N, and Si were investigated using K-Alpha XPS (Thermofisher Scientific, E. Grinstead, UK) and FT-IR (Bruker Optics, MA, USA) techniques. FT-IR measurements were performed at a wavenumber range of 4000–400 cm^{-1} using germanium crystals in an ATR mode (PIKE Technologies, USA).

The morphological and chemical composition analyses of both synthesized Ce-BTC MOFs and NH_2-Ce-BTC MOFs were performed using SEM-EDX (Zeiss Leo 1530, Japan). The SEM was operated at an acceleration voltage of 15 kV, and images were captured using an in-lens detector. The EDX analysis was conducted under the same conditions to determine elemental composition. For the study of chemical bonds and valence states, K-Alpha XPS (Thermo Fisher Scientific, E. Grinstead, UK) was utilized. XPS spectra were acquired with a monochromatic Al Kα X-ray source, operating at 1486.6 eV with a spot size of 400 μm. The analyzer was set to a pass energy of 50 eV for high-resolution scans. Charge compensation was employed, and binding energies were calibrated using the C 1 s peak at 284.8 eV as a reference. Additionally, FT-IR analysis was conducted using a spectrometer (Bruker Optics, MA, USA) in the ATR mode with germanium crystals (PIKE Technologies, USA). Spectra were recorded over a wavenumber range of 4000–400 cm^{-1}. Each spectrum was obtained from an average of 32 scans at a resolution of 4 cm^{-1}, ensuring detailed and reproducible spectral data.

2.3. Membrane fabrication and characterization

The ultra-thin selective layer on porous PES substrates was fabricated through interfacial polymerization (IP) between MPD and TMC [24]. To prepare TFC membranes, PES substrates were first immersed in a 1 wt% MPD solution containing 0.2 wt% SDS and 1 wt% TEA for 5 min. Excess MPD solution was removed using a roller before adding 0.4 wt./v% TMC solution to the membrane surface for 30 s to complete the interfacial polymerization reaction (referred to as TFC membranes without MOFs). The same procedure was followed for TFN membranes containing Ce-BTC and NH_2-Ce-BTC nanomaterials, except MOFs were added to the MPD solution at concentrations of 250, 500, and 1000 mg/L. In an ice bath, the mixture was stirred for 10 min and ultrasonicated for 6 min. After selective layer formation, membranes were heat-cured at 60 °C for 4 min and stored in 20 °C deionized water before testing. Ce-BTC and NH_2-Ce-BTC TFN membranes with concentrations of 250, 500, and 1000 ppm were designated as Ce-BTC-250, Ce-BTC-500, Ce-BTC-1000, NH_2-Ce-BTC-250, NH_2-Ce-BTC-500, and NH_2-Ce-BTC-1000, respectively. Table 1 summarizes the labeling formulation of the membranes. Section S.1.1 of the Supporting Information (SI) provides details of the characterization techniques used in this study. Fig. 1 provides an overview of the fabrication process and schematic illustration of membranes and nanoparticles.

2.4. Membranes performance evaluation

A laboratory bench-scale PRO setup shown in Fig. 2 was designed and constructed to evaluate the performance of pristine TFC and TFN membranes for osmotic filtrations. Power density is a measure of the energy production per unit of time and the surface area of the membrane, serving as an indicator of energy production [12]. Further details regarding the setup and methodology used for determining water and reverse solute fluxes, power density, as well as the FO/PRO performance of the membranes can be found in SI. The intrinsic characteristics of the membranes, including solute permeability (B) and water permeability (A) coefficients, were determined following the protocol discussed in our previous study [26,47], which is summarized in the SI. The membrane characteristics were calculated using the average of three separate measurements from three individual experiments.

3. Results and discussion

3.1. Characterization of Ce-BTC and NH_2-Ce-BTC MOFs

The detailed morphological and compositional characterization of the Ce-BTC MOF, both before and after amine-functionalization, is essential for their successful incorporation into polyamide TFC membranes. In this regard, Fig. 3**a** shows the rod-shaped morphologies of Ce-BTC MOFs, with diameters ranging between 80 and 150 nm. These MOFs tend to aggregate into larger bundles after APTES-based amine-functionalization, as indicated by changes in surface chemistry and the EDX detection of 1.6 wt% Si and 2.7 wt% N (**Fig. S2**). FT-IR spectra of synthesized Ce-BTC MOFs and NH_2-Ce-BTC MOFs are displayed in Fig. 3**c.** In the FT-IR spectra of Ce-BTC MOFs and NH_2-Ce-BTC MOFs, the characteristic peaks at 3379, 2820–2930, 1102 cm^{-1} correspond to the

Table 1
The summary of membranes' labeling information.

Membrane	Ce-BTC MOF (ppm) in MPD solution	NH_2-Ce-BTC MOF (ppm) in MPD solution
Ce-BTC-250	250	0
Ce-BTC-500	500	0
Ce-BTC-1000	1000	0
NH_2-Ce-BTC-250	0	250
NH_2-Ce-BTC-500	0	500
NH_2-Ce-BTC-250	0	1000

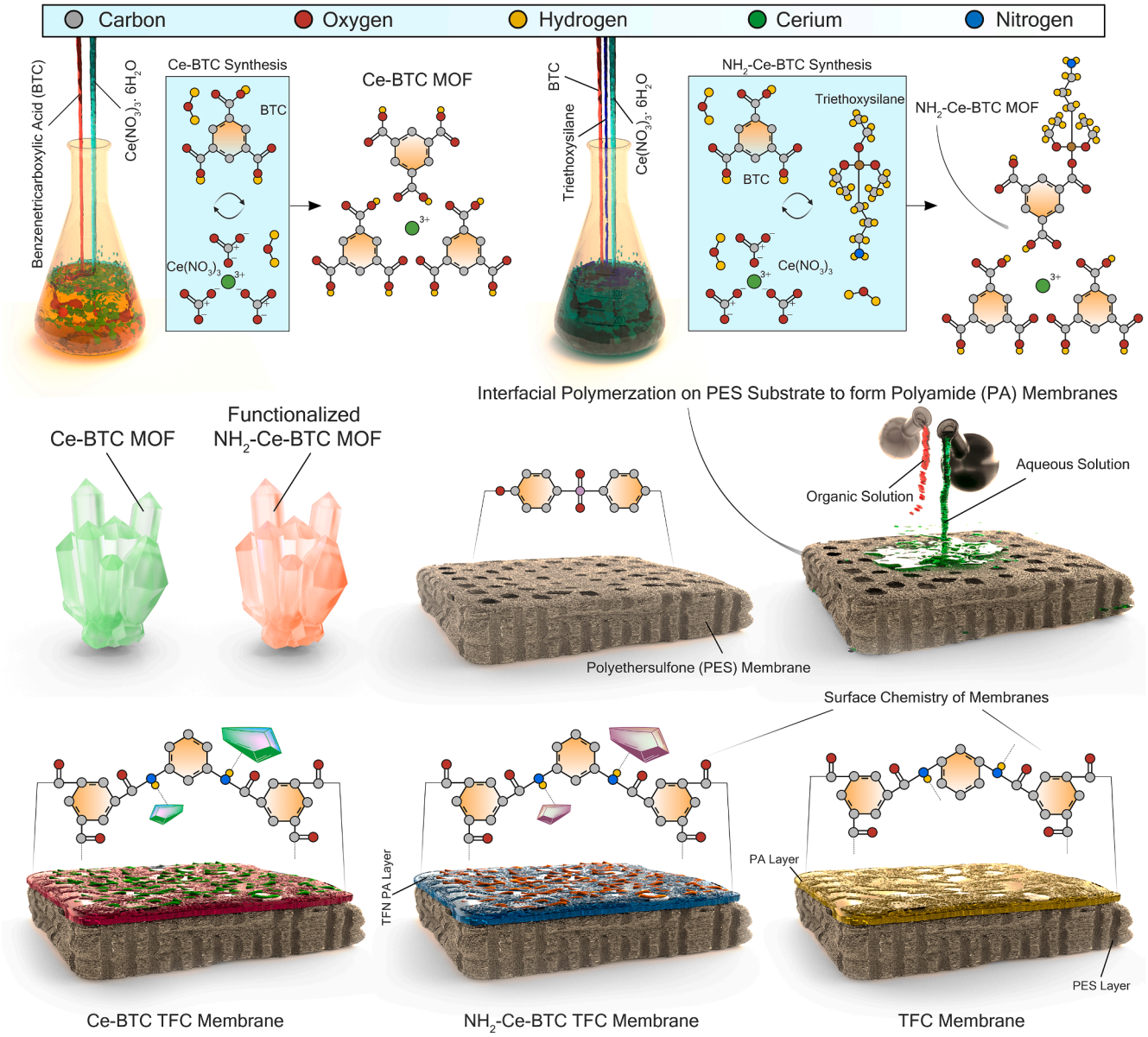

Fig. 1. The schematic illustration of MOFs and TFN membrane fabrication process. The diagram depicts the key stages of MOF formation from precisely coordinated metal ions and organic linkers, emphasizing the importance of modulating synthesis parameters to control MOF characteristics. Following that, the tailored MOFs are integrated into polyamide membrane matrices. To ensure a defect-free MOF-membrane structure, surface conditioning and meticulous interface management techniques are used, emphasizing the importance of material integration and structural integrity. The figure captures the project's dual goals: optimizing MOF properties to facilitate targeted separation and improving membrane performance parameters (e.g., permeability, selectivity, and power generation). The figure illustrates the meticulous balance between material synthesis, microstructural management, and functional optimization in the domain of advanced separation technologies.

stretching vibration of O-H, C-H, and C-O-C/C-O bonds [48]. The small peaks below 660 cm^{-1} are attributed to the stretching vibration of Ce-O links. The sharp peaks located at the ranges of 1320–1420 cm^{-1} and 1510–1630 cm^{-1} are assigned to the symmetric and asymmetric tensile vibration of carboxylate ions [49]. In the spectrum of NH_2-Ce-BTC MOFs, the appearance of new characteristic peaks at 1024, 1479, and 1174 cm^{-1} are linked to the stretching vibration of Si-O and N-H bonds and bending vibration of C-H bonds of the grafted APTES molecules, respectively [49]. FT-IR results confirmed the coordination of Ce ions with trimesic acid ligands and successful APTES grafting.

The XPS analysis in Fig. 3**d–h** offers a more thorough understanding of the atomic valent states in Ce-BTC and NH_2-Ce-BTC MOFs. Successful APTES grafting is indicated by the emergence of new N 1 s and Si 2p signals in NH_2-Ce-BTC MOFs, alongside the distinct signals of C 1 s, O 1 s, and Ce 3d observed in Ce-BTC MOFs (see Table 2). The deconvoluted peaks O 1 s, Ce 3d, N 1 s, and Si 2p provide insights into various bond types and oxygenated functionalities of organic trimesic acid ligands. Additional confirmation of the existence of amino-silane molecules in NH_2-Ce-BTC MOFs comes from alignment with EDX and FT-IR results. The sedimentation behavior of Ce-BTC MOFs and NH_2-Ce-BTC MOFs in different media (Fig. 3**i**) confirms that amine-functionalization improves stability and dispersion. The compatibility and dispersibility of Ce-BTC MOFs are improved by this crucial modification, which is advantageous for many applications. More detailed characterization of MOFs can be found in section 2.1 of SI (S2.2.).

SEM-EDX, FT-IR, and XPS analyses indicate that amine-

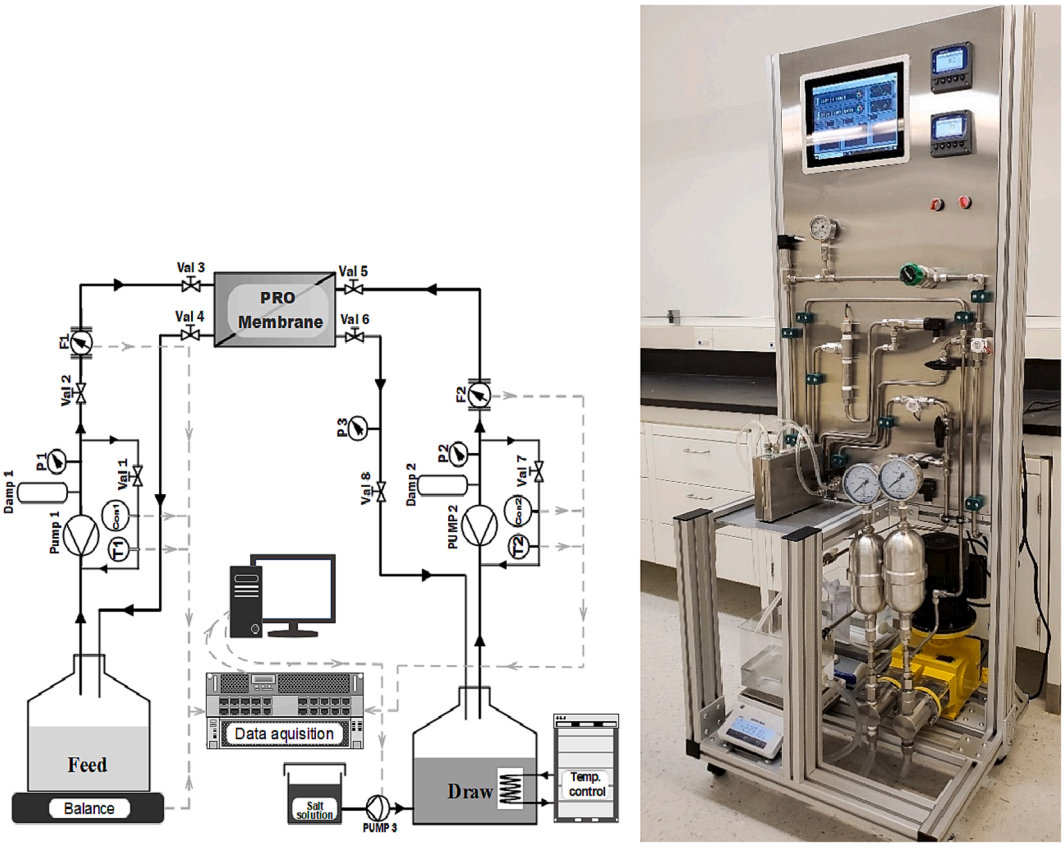

Fig. 2. Schematic description of the laboratory PRO experimental setup.

functionalization changes the surface energy and chemical properties of the MOFs. This modification is crucial for achieving a homogeneous dispersion of these nanomaterials within the polyamide matrix, reducing membrane defects and irregularities that could impair PRO membrane performance. Furthermore, the improved dispersion stability of the NH_2-Ce-BTC MOFs in various media, as evidenced by sedimentation studies, implies their enhanced potential to maintain structural integrity during PRO operation. These characteristics could potentially improve mechanical resilience, antifouling capabilities, and osmotic performance, all of which are critical for the realization of efficient and robust PRO membrane applications.

3.2. Surface characteristics of the membranes

Fig. 4 depicts the surface chemistry analysis of TFC and TFN membranes using ATR-FTIR spectroscopy. The peak observed at 1485 cm^{-1} corresponds to the C–C stretching vibrations in the aromatic rings, and the peaks at 1300 and 1320 cm^{-1} are related to the stretching vibrations of O═S═O [39,47]. Furthermore, peaks at 1145 and 1245 cm^{-1} are attributed to the PES substrate's phenyl ring and asymmetric C-O-C group, respectively [52]. In all spectra, the signature peaks of the PA layer can be discerned at 1540 cm^{-1} (coupled C-N and N-H bending stretching vibration of amide II), 1660 cm^{-1}(amide I, stretching vibration of C═O), and 1610 cm^{-1} (N–H of amide) [14]. Compared with the TFC membrane, a higher level of the N–H stretching and the carboxyl group (C═O bond) in the TFN membranes enhanced the intensity of the distinctive PA peaks. The emergence of slightly intense peaks around 1440 cm^{-1} and 1374 cm^{-1} is likely a consequence of potential interactions between MOFs and the polyamide network, as these peaks were absent in the blank TFC membrane spectrum [52]. In the case of NH_2-Ce-BTC TFN membrane, increased intensity of the peak at 1200 cm^{-1} and 669 cm^{-1} is attributed to the C-N stretching and N-H bond, respectively, present in the amine-functionalized MOF structure [53]. The deformation of bonds at 1044 cm^{-1} for both Ce-BTC and NH_2-Ce-BTC TFN membranes suggest possible interactions between nanomaterials and the PA network, which are not evident in the TFC membrane spectrum [26]. Finally, the ATR-FTIR analysis confirms the successful incorporation of MOFs, including the amine-functionalized Ce-BTC, into the TFN membranes. The changes in peak intensities and the appearance of new peaks indicate strong interactions between the MOFs and the polyamide network, implying their successful integration with the PA matrix. These alterations in the membrane chemistry can influence water permeation, solute rejection, and fouling resistance, which are critical factors in osmotic filtrations. The amine-functionalized MOF structure, characterized by the C-N stretching and N-H bond, may enhance membrane selectivity and increase water flux due to the increased hydrophilicity of the membrane surface. Furthermore, the interactions between MOFs and the PA network can change membrane morphology, potentially resulting in increased surface roughness and mass transfer, thereby improving the performance of FO and PRO processes.

The surface roughness of the fabricated membranes was evaluated using AFM, and the obtained roughness parameters, average roughness (Ra), and root-mean-squared roughness (Rq) are presented in Fig. 4**b–c**. The incorporation of MOFs into the PA layer changes the surface morphology of the membrane, leading to an increase in surface roughness, as observed by SEM. The pristine TFC membrane had an average roughness (Ra) of 93.9 nm and a root-mean-squared roughness (Rq) of 112.8 nm, while the Ce-BTC-500 and NH_2-Ce-BTC-500 TFN membranes had Ra values of 105.2 nm and 116.8 nm, and Rq values of 126.1 nm and 137.8 nm, respectively. The amount and size of MOF nanorods within the PA layer influence the extent of surface roughness enhancement [26]. The increase in surface roughness can enhance turbulence near the membrane surface, potentially improving mass transfer and decreasing

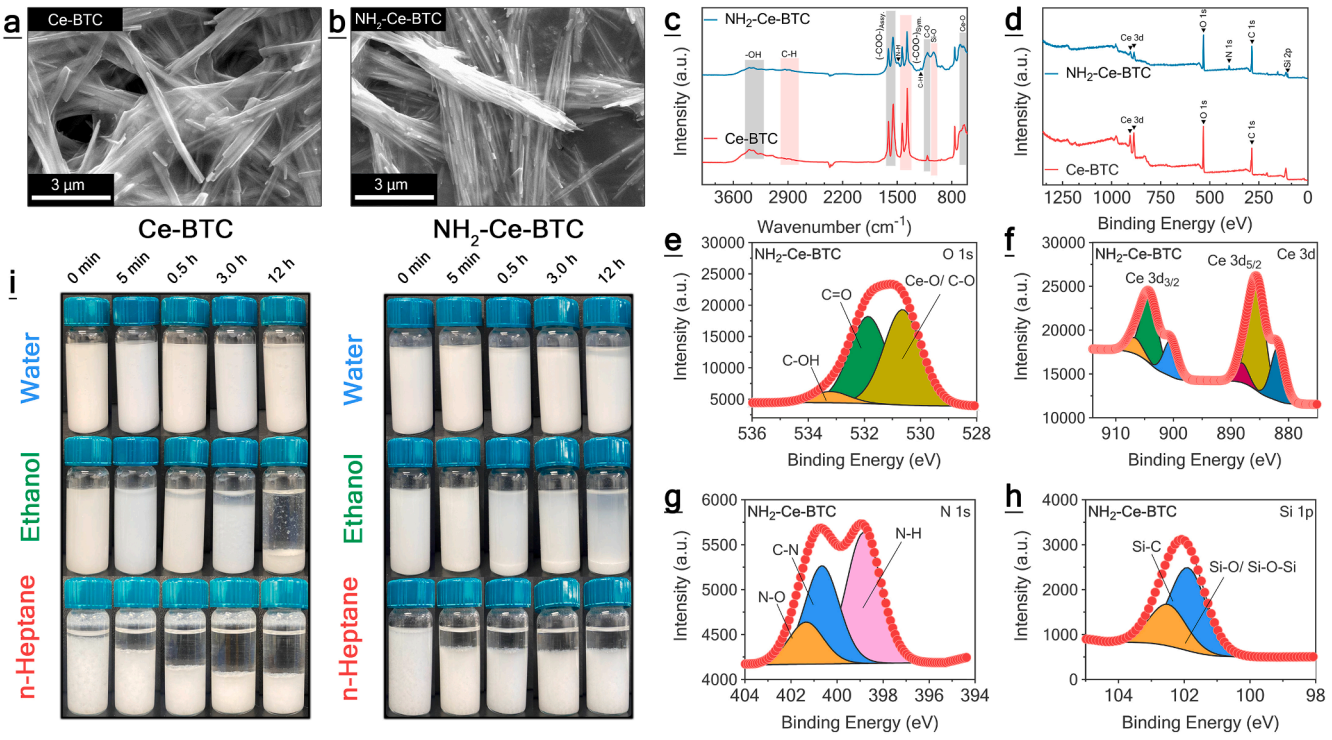

Fig. 3. (a and b) SEM images of Ce-BTC and NH2-Ce-BTC MOFs. (c) FT-IR spectra of synthesized Ce-BTC MOFs and NH2-Ce-BTC MOFs. (d) Full-range XPS spectra of synthesized Ce-BTC MOFs and NH2-Ce-BTC MOFs and the high-resolution XPS spectra of (e) O 1s, (f) Ce 3d, (g) N 1s, and (h) Si 2p signals for NH2-Ce-BT MOF. (i) The sedimentation behavior of Ce-BTC MOFs and NH2-Ce-BTC MOFs in water, ethanol, and n-heptane at various times. These nanomaterials have a bundle-like rod morphology with an average 80–150 nm diameter. New N1s and Si2p signals in NH2-Ce-BTC MOFs confirm APTES grafting, and XPS spectra show characteristic atomic valent states. Improved stability and dispersion following amine-functionalization are further validated by changes in sedimentation behavior in various media.

Table 2
Deconvoluted data related to the O 1s, Ce 3d, N 1s, and Si 2p signals for NH2-Ce-BTC MOFs.

Signal	Corresponded to	B.E. (eV)	FWHM (eV)	Ref.
O 1s	Ce-O/C-O	530.6	1.58	[50,51]
	C = O	531.9	1.58	
	C-OH	533.2	1.58	
Ce 3d	Ce $3d_{5/2}$	878–891	–	[50,51]
	Ce $3d_{3/2}$	897–910	–	
N 1s	N-H	398.8	1.79	[49]
	C-N	400.6	1.79	
	N-O	401.3	1.79	
Si 2p	Si-C	101.9	1.33	[49]
	Si-O/Si-O-Si	102.5	1.33	

concentration polarization [54,55]. This, in turn, can lead to improvements in water flux and reduced energy consumption during the filtration process [56]. However, it is essential to note that increased roughness may also contribute to a higher propensity for fouling. Therefore, optimizing the membrane surface properties is crucial to strike a balance between these competing factors and achieve improved performance in water purification and power generation processes [57].

The surface wettability of the membranes was assessed using water contact angle measurements, and the results are shown in Fig. 4**d**. The average contact angle decreased significantly, from 81.3° for the pristine TFC membrane to 62.4° and 55.2° for the Ce-BTC and NH_2-Ce-BTC membranes, respectively. This reduction indicates enhanced hydrophilicity due to the successful incorporation of MOFs into the PA active layer. The improved wettability can be attributed to specific hydrophilic functional groups within the MOF structures, such as carboxylate and hydroxyl groups in Ce-BTC and amine groups in NH_2-Ce-BTC [58]. These functional groups facilitate hydrogen bond interactions with water molecules, increasing the membranes' affinity for water [58]. The NH_2-Ce-BTC membrane, particularly, has a more hydrophilic surface than the Ce-BTC membrane, as evidenced by its lower contact angle. This increased hydrophilicity is most likely due to the synergistic effects of the amine and hydrophilic oxygen-containing functional groups present in the NH_2-Ce-BTC structure.

Fig. 4**e** depicts the results of a surface zeta potential analysis conducted over a pH range of 4 to 9. Within this pH range, all membranes exhibited a negative surface charge, which can be attributed to the protonation and deprotonation of carboxylic acid groups in the polyamide structure of the TFC membrane [59]. Polyamide membranes contain weakly acidic COOH groups that, depending on the pH of the solution, can impart a positive or negative charge to the surface. The degree of ionization and the pH of the solution influence the surface charge, which is governed by the equilibrium dissociation reaction of R-COOH (R-COOH ⇔ R-COO^- + H^+) [60]. When nanorod MOFs are incorporated into the polyamide layer, TFN membranes exhibit a more negative surface charge than the control TFC membrane [26]. This increased negative charge can be attributed to the higher carboxylic group content (derived from hydrolyzed COCl groups) in the polyamide layer due to the reduced amide linkages. Furthermore, the oxygen-containing functional groups in MOFs can undergo deprotonation at high pH levels, contributing to the increased negative charge. The slight difference observed in the NH_2-Ce-BTC-500 membrane at lower pH values may be attributed to the deprotonation of the amine groups within the NH_2-Ce-BTC MOF structure, resulting in a marginally less negative charge than the Ce-BTC-500 membrane.

A more negatively charged membrane surface can enhance the performance of FO and PRO processes due to several interconnected factors: (i) The increased hydrogen bonding between the membrane surface and water molecules, facilitated by a more negatively charged surface,

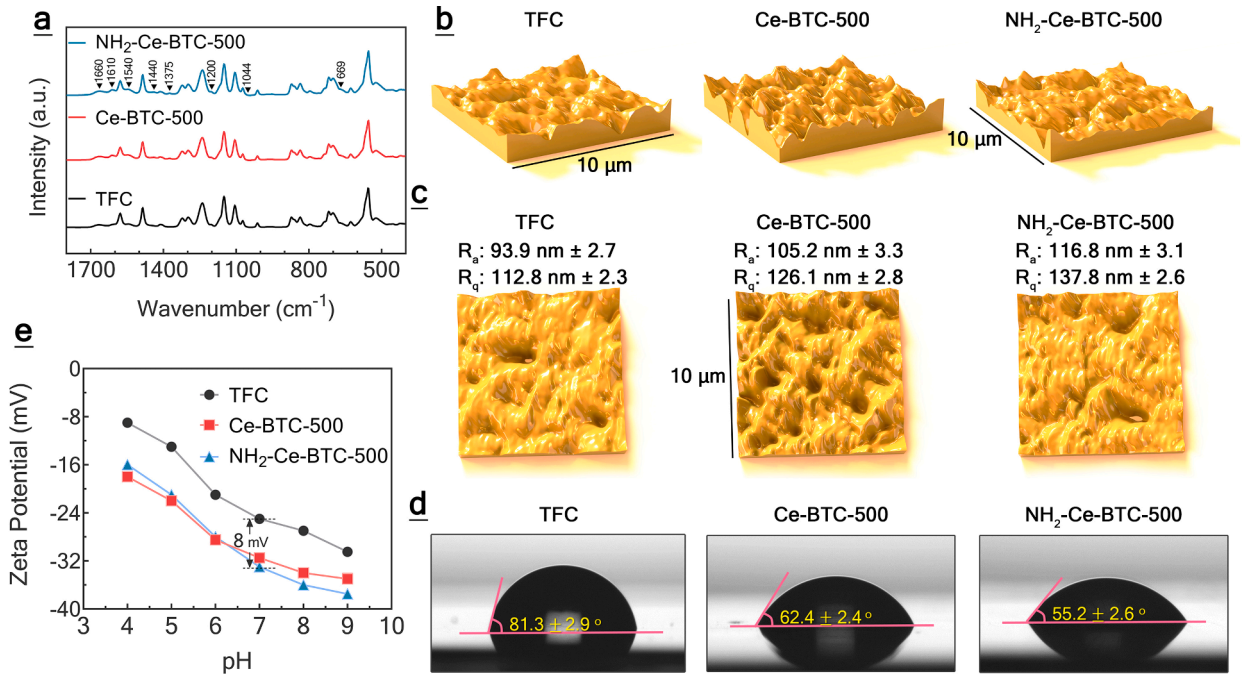

Fig. 4. ATR-FTIR spectra of TFC and TFN membranes, highlighting PA layer and PES substrate peaks. In TFN membranes, increased intensities and additional peaks indicate successful MOF incorporation and potential interactions between MOFs and the polyamide network. Bond deformation at 1044 cm-1 indicates the possibility of nanomaterial-PA interactions, which are not present in the TFC membrane. (a) 3D AFM images presenting the surface morphology of TFC and TFN membranes, along with Ra (average roughness) and Rq (root mean square roughness) parameters. The incorporation of MOF nanorods in TFN membranes leads to increased surface roughness, which may correlate with enhanced water permeability and overall membrane performance in PRO application. (b) Water contact angle measurements indicate improved hydrophilicity for TFN membranes, resulting from the presence of hydrophilic functional groups in MOF nanorods. The increased surface wettability facilitates higher water flux and better performance in the PRO process. (c) Zeta potential analysis across a pH range of 4 to 9 highlights a more negative surface charge for TFN membranes compared to TFC membranes, owing to the deprotonation of carboxylic acid groups and other oxygen-containing functional groups present in MOFs. The negative surface charge could promote selective ion transport and reduce fouling propensity, ultimately enhancing the membrane performance in the PRO process.

promotes the formation of a hydration layer [61,62]. This hydration layer improves water flux by facilitating the transport of water molecules through the membrane [39]. (ii) A higher negative charge on the membrane surface increases its hydrophilicity, resulting in better water permeation and a lower fouling propensity [63]. Hydrophilic surfaces attract and retain less organic foulants and particulate matter, resulting in more stable and efficient membrane performance during the filtrations [62,64]. (iii) The negatively charged surface can also help to reduce concentration polarization, which occurs when solute concentration builds up near the membrane surface, diminishing the effective osmotic pressure difference across the membrane [65]. By promoting electrostatic repulsion between the negatively charged membrane surface and the negatively charged solutes, the membrane can minimize solute accumulation at its surface, thereby reducing concentration polarization and improving filtration performance [66]. (iv) A negatively charged surface repels negatively charged solutes electrostatically, which can improve the membrane's selectivity towards these solutes [67]. The membrane can maintain a high solute rejection rate by preventing these solutes from passing through the membrane, which is critical for optimal FO and PRO performance.

The influence of nanoparticles on the formation of the polyamide layer is a critical factor to consider when incorporating nanoparticles into TFN membranes [68]. Fig. 5 depicts the surface morphology of TFC and TFN membranes examined using FE-SEM. All TFC and TFN membranes had a distinct ridge and valley structure. FESEM images at high magnification revealed the presence of MOF nanorods on the active layer surface of both the Ce-BTC-500 and the NH_2-Ce-BTC-500 membranes. Notably, these nanorods are uniformly dispersed within the polyamide matrix, avoiding significant aggregation, which has been reported with other nanoparticles in the literature [69–71]. Furthermore, it is evident that the polyamide fully encapsulates the MOFs, indicating a perfect integration of Ce-BTC and NH_2-Ce-BTC nanorods within the polyamide layer of TFN membranes at 500 ppm. The homogeneous distribution of Ce-BTC and NH_2-Ce-BTC nanorods within the polyamide layer validates the initial hypothesis of the high level of compatibility between these two phases. The effective dispersion of MOF nanorods within the polyamide structure during the IP reaction is facilitated by their hydrophilic and organic characteristics, leading to enhanced compatibility with the polyamide matrix and preventing interfacial gaps [21]. Hydrophilic functional groups on the MOF nanorods enable the formation of hydrogen bonds with water and other hydrophilic molecules. These groups promote the dispersion of MOFs in an aqueous amine monomer solution, which is used in the IP process. As a result, the MOFs disperse and distribute uniformly within the polyamide structure. Additionally, the organic nature of MOF nanorods contributes to their compatibility with the polyamide matrix. Both polyamides and MOFs consist of organic components with similar molecular structures and functional groups, such as carboxylic acids and amine groups. This structural similarity promotes stronger interactions and chemical bonding between the MOFs and polyamide chains, resulting in a stable and uniformly distributed composite structure.

The cross-sectional TEM images in Fig. 5 show the polyamide TFC membranes' distinctive structure. These images reveal the formation of a sub-200 nm polyamide layer in both TFC and TFN membranes. Notably, the incorporation of MOFs into the polyamide layer of Ce-BTC-500 and NH_2-Ce-BTC-500 membranes is evident in Fig. 5, where the MOF nanorods are observed to be fully encapsulated within the polyamide layer. This observation suggests that the presence of MOFs may contribute to improved membrane performance in pressure retarded osmosis (PRO) applications by minimizing membrane defects. Fig. 5**c**

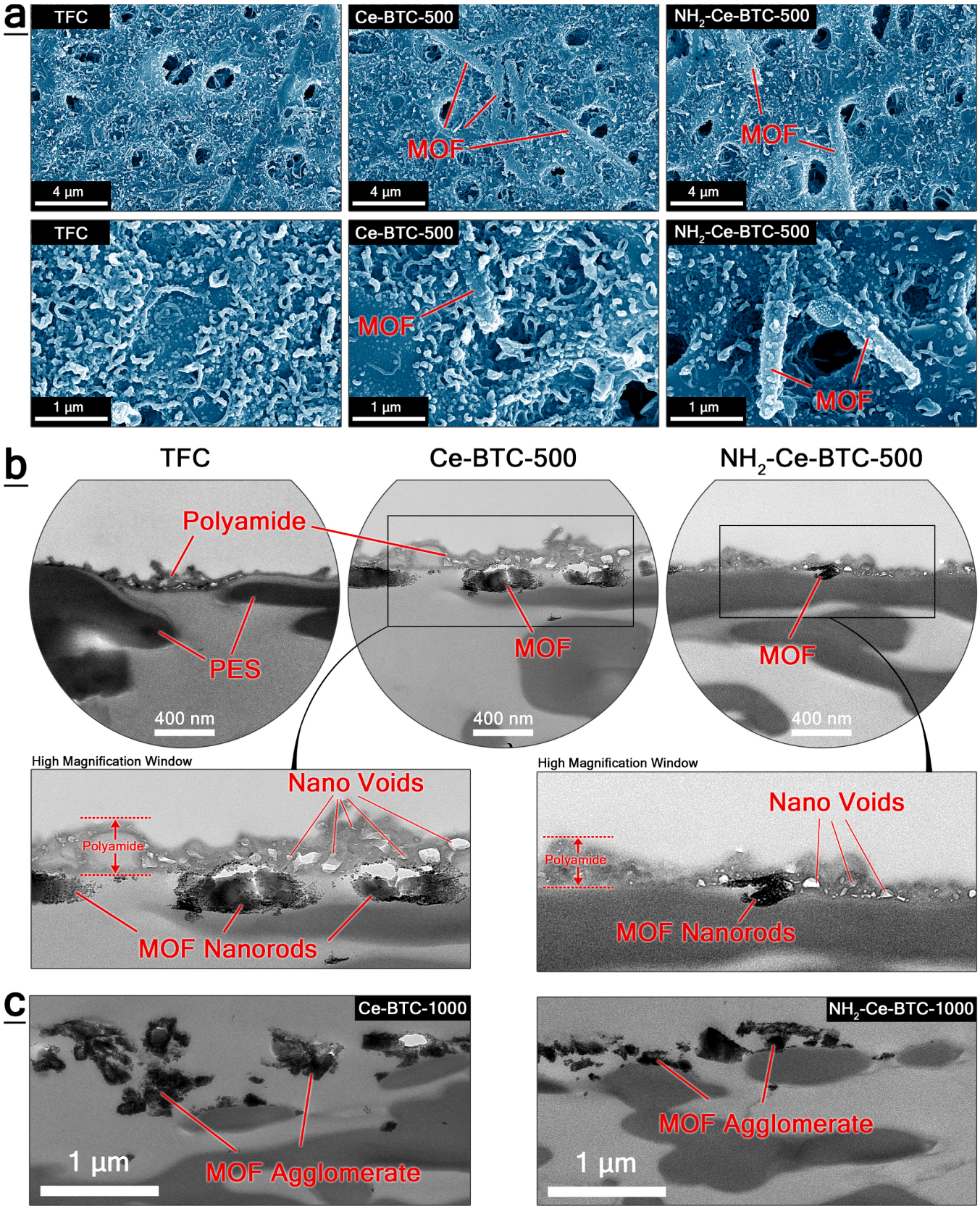

Fig. 5. (a) Top surface FE-SEM and (b) cross-sectional TEM images of TFC and TFN membranes. (c) cross-sectional TEM images of Ce-BTC-1000 and NH2-Ce-BTC-1000 TFN membranes. The images demonstrate the successful integration of MOF nanorods within the polyamide layer, with the amine-functionalized MOFs showing better dispersion and compatibility due to their hydrophilic nature. The modified membranes exhibit a characteristic ridge and valley structure, and the incorporation of MOFs leads to a reduction in the polyamide layer thickness, particularly for NH_2-Ce-BTC membranes. This reduction in thickness contributes to lower resistance to mass transfer, suggesting potential improvements in PRO performance. The TEM images also reveal that the MOF nanorods are entirely encapsulated by the polyamide layer, further emphasizing their effective integration into the membrane structure.

shows TEM images of Ce-BTC-1000 and NH_2-Ce-BTC-1000 membranes containing 1000 ppm MOFs in aqueous solutions. In these images, larger MOF aggregates with dimensions around 500 nm are visible. Although these aggregates are embedded within the polyamide film, their presence raises concerns about potential defects in the selective layer, which could impact filtration efficiency. It is worth noting that larger aggregates are more prevalent in Ce-BTC-1000, implying that amine-functionalized MOFs have a lower tendency for large aggregate formation. This reduced aggregation can be attributed to the NH_2 groups present on the external surfaces of the nanorods, promoting better dispersion in the aqueous solution and a more uniform distribution within the polyamide layer. MOF dispersion may improve membrane performance by increasing water flux and decreasing fouling [72].

Moreover, the TEM images reveal a slight reduction in the thickness of the polyamide layer, particularly noticeable in the NH_2-Ce-BTC membrane. This might be attributed to the increased rate of interfacial polymerization facilitated by the incorporation of hydrophilic MOF nanorods, with a more significant impact observed in the case of NH_2-Ce-BTC nanorods due to their higher hydrophilicity and functional group density [73]. Additionally, the steric hindrance and improved compatibility of MOF nanorods with the amine monomer contribute to the reduced penetration of MPD and the deceleration of polyamide formation, ultimately resulting in a thinner active layer [74,75]. This reduction in polyamide layer thickness can contribute to a lower mass transfer resistance, leading to improved water flux and enhanced performance in pressure retarded osmosis (PRO) [76].

The TEM analysis of the TFN membranes reveals essential details about the successful incorporation of MOF nanorods within the polyamide layer and their size distribution. This data is instrumental when combined with other characterization techniques and membrane performance assessments for PRO applications. The TEM analysis helps in understanding the underlying reasons behind the changes observed in ATR-FTIR peak intensity, as well as the enhancements in hydrophilicity and the negative surface charge of the TFN membranes. These changes collectively lead to improved antifouling and permeation properties, making the TFN membranes highly suitable for PRO applications

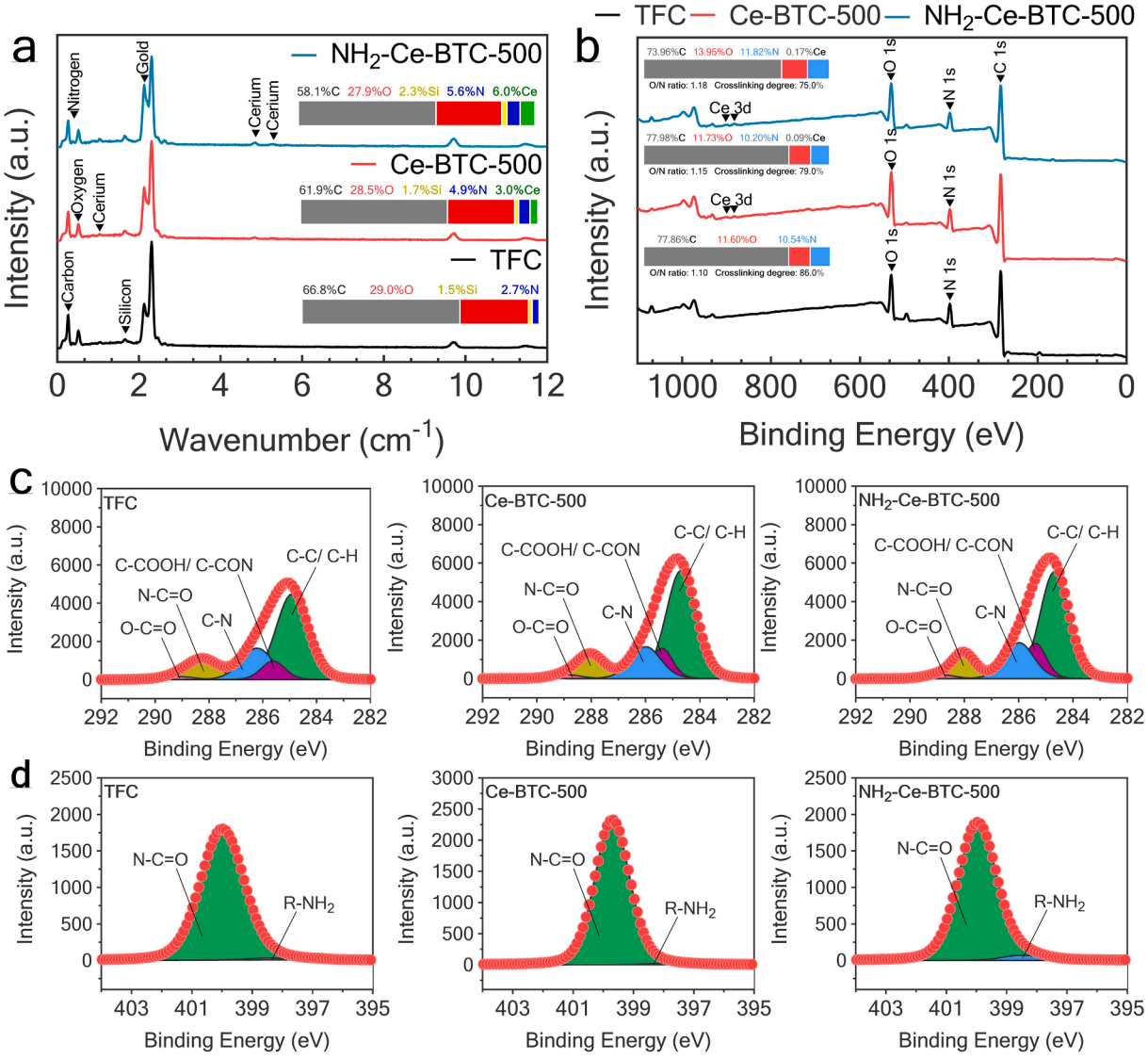

Fig. 6. EDX spectra of the membranes. (b) XPS survey spectra of the TFC and TFN membranes. It should be noted that the other unlabeled peaks correspond to materials utilized during sample preparation (for instance, the peak near 680 eV represents the fluorine employed in the XPS instrument's vacuum process). Deconvoluted high-resolution XPS spectra, (c) C 1s and (d) N 1s for the TFC and TFN membranes. The enhanced Ce atom presence in the NH2-Ce-BTC-500 membrane, which indicates improved dispersion and compatibility with the polyamide matrix, is highlighted by EDX and XPS analyses for Ce-BTC-500 and NH2-Ce-BTC-500 membranes. As a result of steric hindrance, interference with interfacial polymerization, and alternative bonding mechanisms induced by MOF interactions, the associated O/N ratio suggests a reduced degree of cross-linking in the polyamide structure.

[31,77].

Fig. 6 shows EDX spectra and XPS results obtained from Ce-BTC-500 and NH_2-Ce-BTC-500 membranes, revealing a higher concentration of Ce atoms in the NH_2-Ce-BTC-500 sample. This observation aligns with the earlier discussion regarding the superior dispersion of amine-functionalized MOFs attributed to the presence of NH_2 groups on the nanorods' external surfaces. These surface modifications enhance the hydrophilicity of the nanorods and improve their compatibility with the polyamide matrix. Table 3 summarizes the bonds and peaks identified through XPS analysis (a more detailed discussion on the XPS analyses can be found in section 2.2 of SI). The oxygen-to-nitrogen (O/N) ratio indicates the degree of cross-linking in the polyamide structure [47]. A higher O/N ratio typically corresponds to a lower degree of cross-linking in the polyamide network [78]. Several factors contribute to the reduced cross-linking observed upon the addition of Ce-BTC and NH_2-Ce-BTC to the polyamide matrix: (i) The incorporation of MOF nanorods into the polyamide matrix can result in steric hindrance [74,75]. The larger size of the MOF particles interferes with the close packing of polymer chains and the formation of covalent bonds between them. This steric hindrance can cause the cross-linking process to be disrupted, resulting in a less cross-linked polyamide structure. (ii) The presence of MOFs in the aqueous amine solution can disrupt the interfacial polymerization process. This can weaken the intermolecular linkages between functional groups of the monomers, i.e., the amine terminal of the MPD and the acyl chloride functional group of the TMC, resulting in a less cross-linked polyamide structure [47,79]. (iii) During the interfacial polymerization process, interactions between MOFs and the functional groups of MPD or TMC monomers can lead to the formation of alternative chemical bonds that differ from the conventional polyamide chain cross-linking, thereby decreasing the overall degree of cross-linking [80–82]. Particularly, in the case of NH_2-Ce-BTC, the amine functional groups on the surface of the MOF nanorods may react with the TMC's acyl chlorides, which diminishes conventional polyamide crosslinking [39].

3.3. Evaluation of optimal MOF loading rates in membranes

The concentration of MOFs within the membrane structure significantly impacts membrane performance. Developing high-performing and efficient membranes for various filtration applications requires precise optimization of MOF concentration. However, finding the right balance is crucial, as excessive MOF loading can lead to unfavorable outcomes such as nanoparticle aggregation and increased transport resistance. With these considerations in mind, the objective of the current study is to investigate how MOF concentration impacts the functionality of TFC membranes. Fig. 7 shows the filtration results of the TFC and TFN membranes at various concentrations of MOFs in two distinct configurations: active layer facing feed solution (AL-FS) and active layer facing draw solution (AL-DS). It can be seen that in both configurations, Ce-BTC-500 and NH_2-Ce-BTC-500 had higher water flux than Ce-BTC-1000 and NH_2-Ce-BTC-1000. For instance, incorporating 500 ppm Ce-BTC and NH_2-Ce-BTC nanorods within the polyamide layer led to a significant enhancement in water flux, accompanied by a slight increase in reverse salt flux. In the AL-FS configuration with a 2 M NaCl draw solution, the TFC membrane showed a notable increase in water flux values, reaching 42 LMH and 47 LMH for Ce-BTC-500 and NH_2-Ce-BTC-500 membranes, respectively. Similarly, the reverse salt flux exhibited a marginal increase from 4.78 gMH for the TFC membrane to 6.28 gMH and 6.20 gMH for Ce-BTC-500 and NH_2-Ce-BTC-500 membranes, respectively. Likewise, in the AL-DS configuration with a 2 M NaCl draw solution, the TFC membrane demonstrated enhanced water flux values, reaching 50 LMH and 54 LMH for Ce-BTC-500 and NH_2-Ce-BTC-500, respectively. Additionally, the reverse salt flux experienced a slight increase from 4.52 gMH for the TFC membrane to 6.13 gMH and 6.89 gMH for Ce-BTC-500 and NH_2-Ce-BTC-500 membranes, respectively. Conversely, concentrations of MOFs over 500 ppm resulted in a reduction of water flux, likely due to the aggregation of nanoparticles and their poor dispersion in the top polyamide layer [83]. This can thicken the selective layer and increase resistance to water permeation, consequently decreasing water flux [14]. Since concentrations above 500 ppm did not produce the desired balance between water and reverse salt flux, they were not selected for further power density and filtration tests.

3.4. Membranes' power generation performance and osmotic filtrations

Innovative techniques such as the PRO process offer promising opportunities for efficient renewable energy production. The TFN membranes used in this study, specifically those that contain the MOFs Ce-BTC-500 and NH_2-Ce-BTC-500, provide remarkable power density that can be attributed to their excellent permselectivity. Fig. 8 displays the PRO performance of both TFC and TFN membranes, tested at a temperature of 25 ± 0.5 °C across an applied pressure range of 0 to 8 ± 0.1 bar. Given that the burst pressure of the membranes falls within the range of 8 to 9 bar, the power density evaluation was conducted up to a hydraulic pressure threshold of 8 bar. It is expected that water flux passing through the membrane would slightly decrease as the hydraulic pressure increases. Fig. 8**a–c** depicts the water fluxes (J_w), reverse salt flux (J_s), and specific solute flux (J_s/J_w values) of TFC and TFN membranes in the PRO process. The incorporation of MOF increased J_w by approximately 61 % and 83 % for Ce-BTC-500 and NH_2-Ce-BTC-500 membranes, respectively, compared with pristine TFC. Concurrently, the J_s/J_w values of both TFN membranes were lower than that of the pristine TFC. Notably, NH_2-Ce-BTC-500 provided the lowest J_s/J_w ratio, which aligns with its higher flux and similar salt permeability. This suggests that TFN membranes provide better performance (higher flux) in the PRO process without compromising membrane selectivity.

Fig. 8**d** compares the experimental power density as a function of the pressure differential across the TFC and TFN membranes. As the transmembrane hydraulic pressure difference (ΔP) increases, water flux decreases and the power density of both TFC and TFN membranes increases, representing the typical behavior observed in PRO membranes [84]. The overall power density of the TFN membranes containing 500 ppm of Ce-BTC and NH_2-Ce-BTC exhibited higher values than the pristine TFC membrane. The TFC membrane showed a peak power density of 3.3 W/m^2 at 8 bar hydraulic pressure. However, the Ce-BTC-500 and NH_2-Ce-BTC-500 membranes achieved maximum power densities of 6.0 and 6.9 W/m^2, respectively, at the same hydraulic pressure. These results surpass previously reported power densities of PRO membranes and exceed the benchmark of 5 W/m^2 required for the

Table 3
Elemental compositions and significant peak characteristics of the TFC and TFN membranes derived from the XPS spectra.

	Atomic Concentration (%)						C 1S Species (%)						N 1S species (%)	
Membrane	**C**	**O**	**N**	**Ce**	O/N ratio	**Cross-Linking Degree (%)**	C–H, C–C	C–COO, C–CON	–CN–	N–C=O	O–C=O	O - C = O / N - C = O	N–C=O	C-NH_2
Blank	77.86	11.60	10.54	–	1.10	86	55.90	8.89	20.55	12.58	1.98	6.35	98.75	2.25
Ce-MOF-500	77.98	11.73	10.20	0.09	1.15	79	58.17	11.47	17.14	11.21	2.03	5.52	98.70	1.30
NH_2-Ce-MOF-500	73.96	13.95	11.82	0.17	1.18	75	55.57	13.59	18.70	10.07	2.06	4.90	94.42	5.58

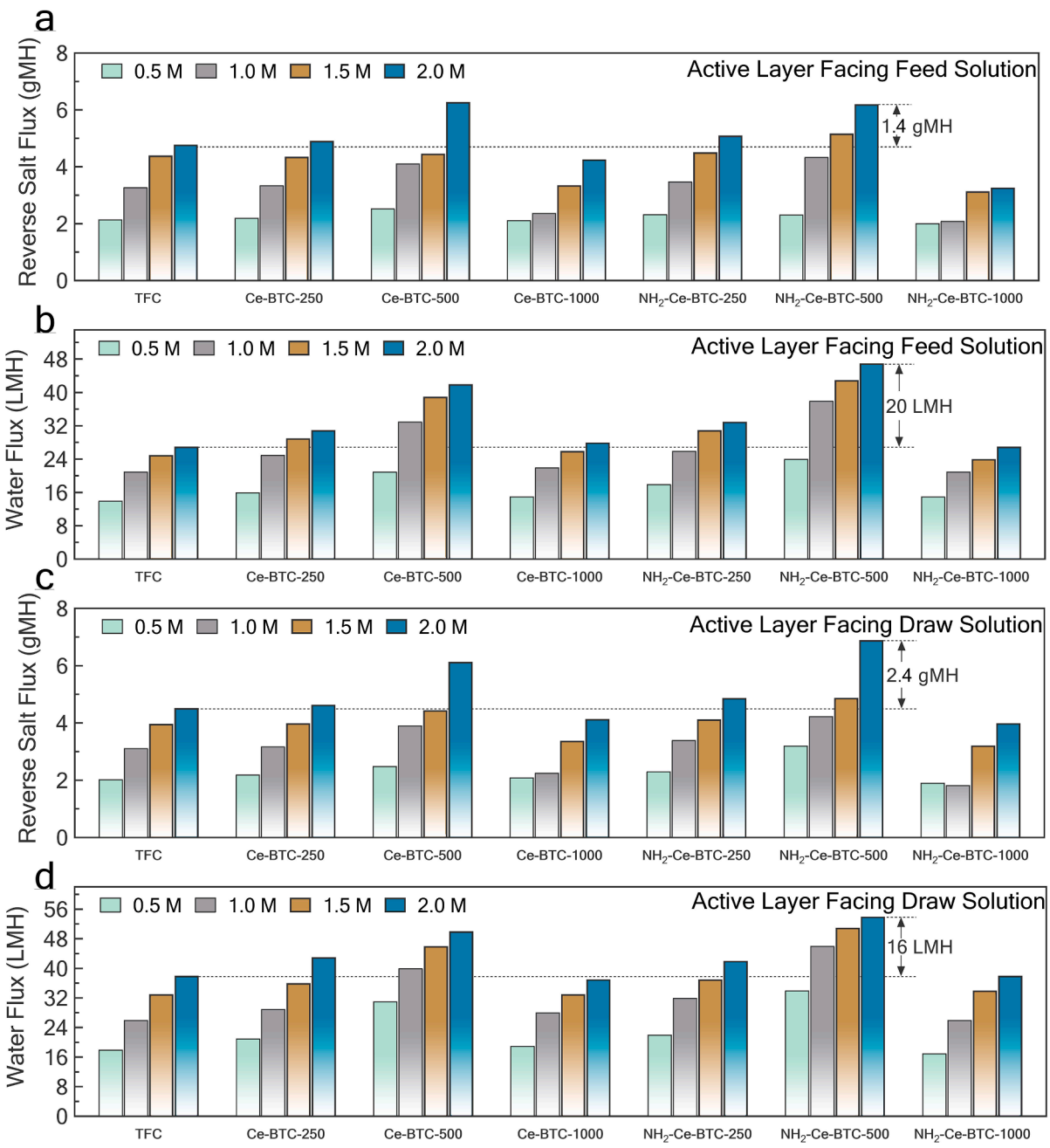

Fig. 7. (a) Water flux and (b) reverse salt flux in AL-FS configuration, (c) Water flux and (d) reverse salt flux in AL-DS configuration for TFC and TFN membranes containing different concentrations (250, 500, and 1000 ppm) of MOFs. Filtration performance of TFC and TFN membranes with varying MOF concentrations, demonstrating enhanced water flux with 500 ppm Ce-BTC and NH2-Ce-BTC nanorods in both AL-FS and AL-DS configurations. MOF concentrations above 500 ppm, on the other hand, reduced water flux due to nanoparticle aggregation and increased transport resistance.

economic viability of the PRO process [85,86]. The trend of increasing power density with applied pressure was consistently observed across all membranes up to a certain pressure threshold, beyond which it started to decrease once the pressure reached the burst pressure of 9 bar. It is worth noting that all membranes examined in this study have free-standing commercial support layers, and the performance decline observed at high pressures may be attributed to the deformation of the thin polyamide layer due to the elongation of the support layer [87,88]. During the PRO process tests, a porous spacer supported the membranes.

The long-term operation of the membranes was evaluated by monitoring its water fluxes (J_w), specific solute flux (J_s/J_w values), and power density (W) at a pressure 8 bar for 8 h with their results present in Fig. 9**a–c**. At a pressure of 8 bar (below burst pressure), where the peak power density was achieved, the membranes are able to maintain a flux of 15 ± 0.3 LMH, 27 ± 0.5 LMH, and 31 ± 0.5 LMH for TFC, Ce-BTC-500, NH_2-Ce-BTC-500 respectively. Similarly, the power densities of the membranes remained unchanged throughout the entire operation period, recorded as 3 ± 0.1 W/m^2 for TFC membrane, 6 ± 0.1 W/m^2 for Ce-BTC-500 membrane, and 6.9 ± 0.1 W/m^2 for NH_2-Ce-BTC-500 membrane. Additionally, the specific solute flux remains unchanged during the test period. However, upon increasing the pressure above 8 bar, a notable increase in the specific salt flux was observed, attributed to membrane deformation as the burst pressure neared 9 bar [89,90]. These findings provide valuable insights into the membranes' behavior under continuous high-pressure conditions.

A comprehensive understanding of these TFN membranes' water flux

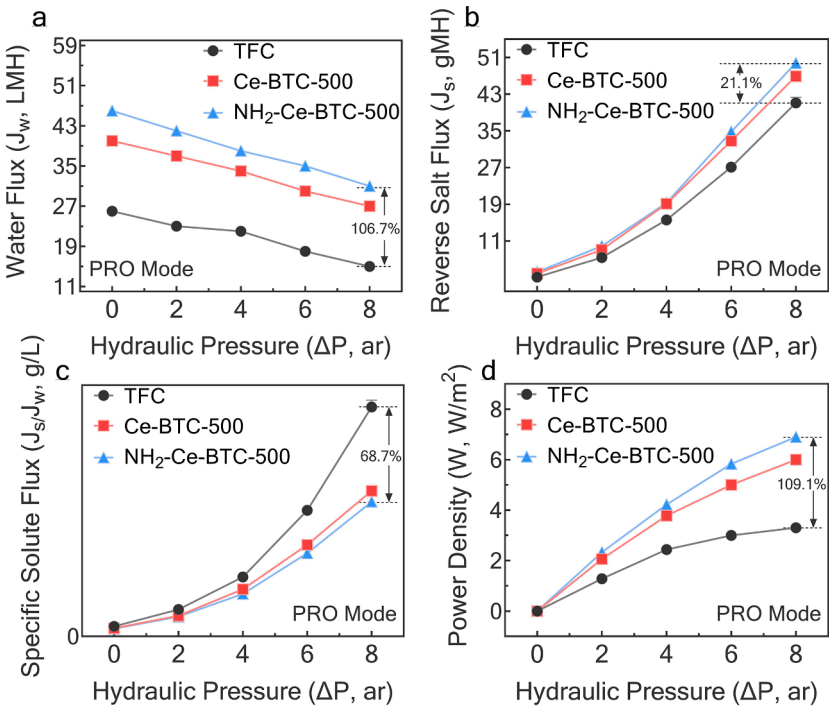

Fig. 8. (a) Water flux (J_w), (b) reverse salt flux (J_s), (c) specific solute flux (J_s/J_w), and (d) power density (W) of the TFC and TFN membranes in the PRO process. PRO performance was measured using DI water feed, and 1.0 M NaCl draw solution. The horizontal dashed line in panel d denotes the industrial objective of achieving commercial viability in the PRO process.

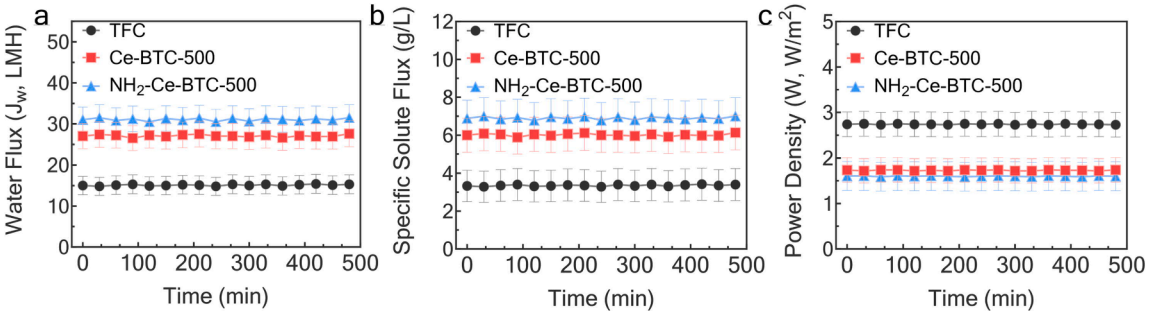

Fig. 9. Long term PRO performance of the TFC and TFN membranes. (a) water fluxes (J_w), (b) specific solute flux (J_s/J_w), and (c) power density (W); (Testing condition: DI water as feed,1.0 M NaCl as draw solution, 25 ± 0.5 °C, 8 bar, and dosing every 15–60 min to regulate the conductivity).

and selectivity can be obtained by comparing their performance in the PRO process and FO filtration under the same conditions. The enhanced power densities observed in the PRO tests can be better interpreted in light of this knowledge. In the PRO process, water flux and power density are directly correlated, and insights gained from FO filtration tests are crucial for understanding how effectively the membranes transport water. Furthermore, by comprehending the behavior of these membranes during FO testing, we can leverage that knowledge to optimize their design and functionality, directly impacting power generation in the PRO process. To thoroughly analyze these novel TFN membranes and their potential in renewable energy applications, it is essential to integrate FO filtration tests with PRO evaluations.

Fig. 10**a and b** present the water flux of TFC and TFN membranes under various draw solution concentrations in two distinct configurations, AL-FS and AL-DS, in FO filtration. The increase in water flux with higher draw solution concentration in both configurations can be attributed to the elevated osmotic driving force. However, at higher NaCl concentrations, the water flux shows a non-linear increase with a reduced slope due to the accumulation of sodium and chloride ions on the polyamide layer within the support layer in the AL-FS configuration, giving rise to internal concentration polarization (ICP). In the case of AL-DS, external concentration polarization (ECP) of the polyamide layer becomes significant due to the high salt concentration of the draw solution [14]. In both cases, the accumulation of salt ions decreases the effective osmotic pressure gradient across the membranes, which becomes more pronounced at higher draw solution concentrations [91]. Moreover, the water flux is higher in the AL-DS configuration compared to the AL-FS configuration, indicating that ICP substantially affects the effective osmotic driving force in AL-FS relative to ECP in AL-DS. These results suggest that the incorporation of MOF nanorods into the polyamide active layer enhances the water flux (J_w) of TFN membranes. Furthermore, Fig. 10**c** demonstrates that TFN membranes' reverse salt flux (Js) is slightly higher than that of the TFC membrane. This can be attributed to the formation of a less dense polyamide structure from incorporating MOF nanorods, as indicated by the XPS results in Table 3. In general, the specific solute flux (J_s/J_w) is an important performance parameter for TFC membranes, where a lower value of J_s/J_w is desirable to achieve greater water flux and selectivity [92]. The J_s/J_w values for the TFC and TFN membranes are presented in Fig. 10**d**. The TFN membranes exhibit a reduction in J_s/J_w, suggesting a considerable

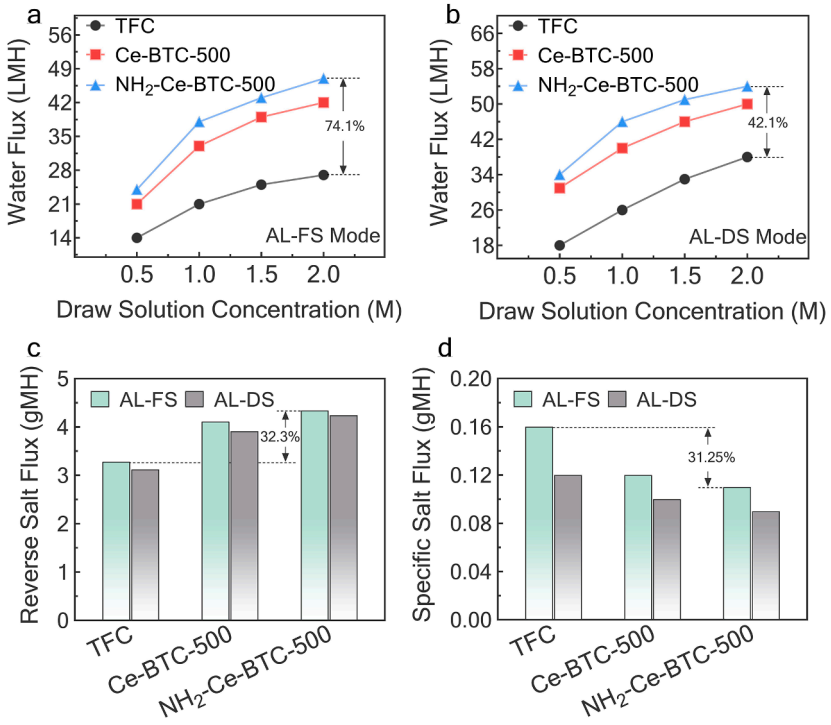

Fig. 10. (a) Water flux in AL-FS configuration, (b) Water flux in AL-DS configuration, (c) reverse salt flux, (d) specific salt flux for TFC and TFN membranes.

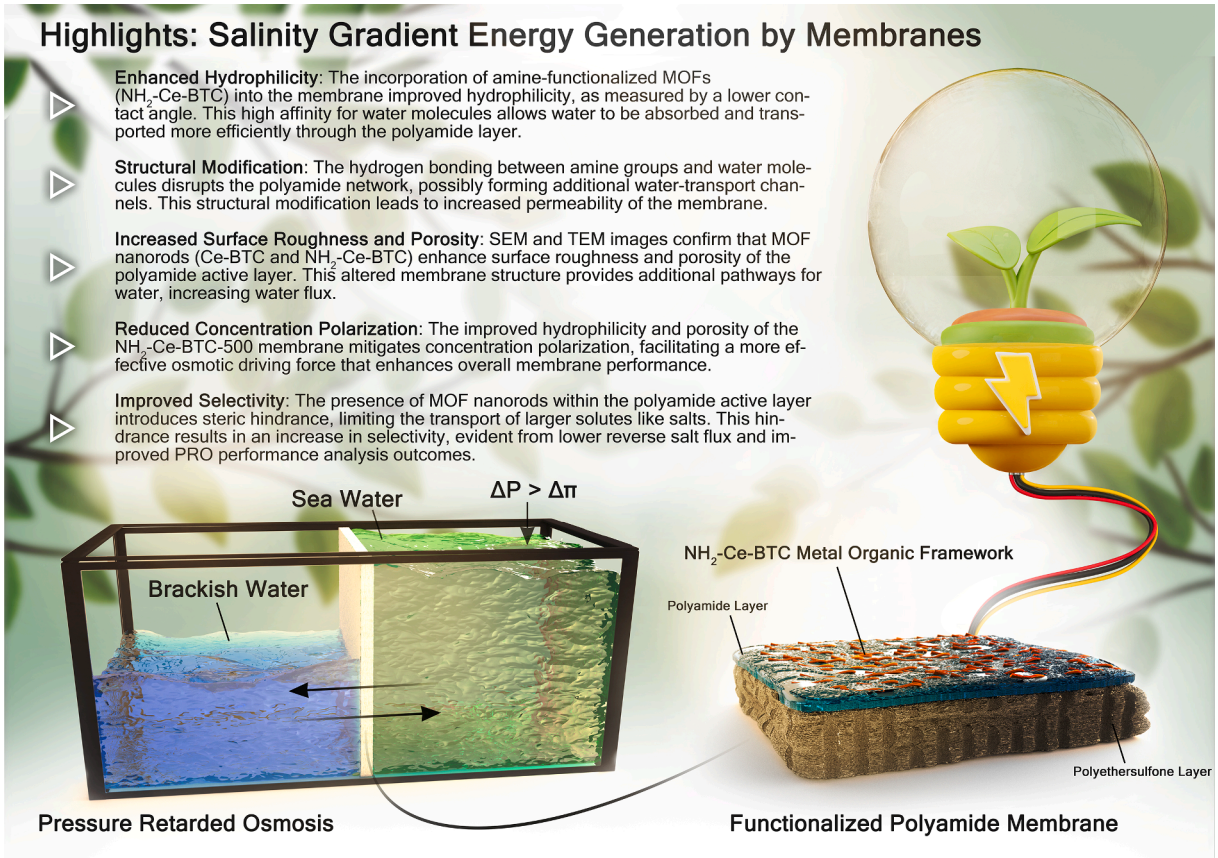

Fig. 11. Schematic summary of the main factors playing a role in the performance of membranes for the osmotic power generation process. Improved hydrophilicity from amine-functionalized MOFs, modified membrane structure creating additional water-transport channels, Increased surface roughness and porosity confirmed by SEM and TEM, reduced concentration polarization enhancing osmotic driving force, and increased selectivity due to steric hindrance by MOF nanorods all contribute to the improved performance of NH2-Ce-BTC-500.

improvement in water transport and selectivity for TFN membranes, with slightly better results observed for NH_2-Ce-BTC-500 membrane. A more detailed discussion on the influence of nanomaterial incorporation on transport parameters of water permeability (A), solute permeability (B), and structural parameter (S) for the TFC and TFN membranes can be found in SI section S3.

Fig. S3 shows digital photographs of NH_2-Ce-BTC-500 membrane after undergoing PRO and FO processes. The images reveal that during the FO process, the support-polyamide assembly of the membrane maintained a flat shape. In contrast, it was compressed and inserted into the gaps of the spacer mesh, a phenomenon commonly referred to as the "shadow effect," as reported in the study conducted by Kim et al. [93]. This effect may contribute to the partial blockage of water transport pathways across the membranes. Moreover, the support-polyamide assembly became detached and extended into the cell flow channel, causing tension on the membrane, which could potentially lead to changes in permselectivity [88]. The membrane's selectivity may also be compromised due to minor defects, thereby reducing the osmotic pressure gradient and water flux [94].

3.5. Discussion

After conducting a comprehensive analysis of the membrane characterization and performance in osmotic filtrations, it was observed that the NH_2-Ce-BTC-500 membrane exhibited superior performance compared to the Ce-BTC-500 and pristine TFC membranes. Fig. 11 provides a schematic summary of the key factors influencing the enhanced performance of the NH_2-Ce-BTC-500 membrane in the osmotic power generation process. The improved performance can be attributed to the following factors, which are supported by the aforementioned characterizations:

(a) The incorporation of amine-functionalized MOFs (NH_2-Ce-BTC) within the polyamide layer significantly impacted the hydrophilicity of the membrane, as evidenced by the contact angle measurements. Compared to the Ce-BTC-500 and pristine TFC membranes, the NH_2-Ce-BTC-500 membrane exhibited a lower contact angle, indicating a higher affinity for water molecules. The amine groups present in the NH_2-Ce-BTC-500 membrane, consisting of nitrogen atoms with lone pairs of electrons and hydrogens, can form hydrogen bonds with water molecules. Such an enhanced affinity for water increased the membrane's hydrophilic nature, thereby facilitating the rapid absorption and transport of water through the polyamide layer of the membrane.

(b) SEM and TEM images confirmed that incorporating MOF nanorods (Ce-BTC and NH_2-Ce-BTC) into the polyamide layer increased surface roughness and porosity. This modified membrane structure provided additional pathways for water to pass through, increasing PRO process water flux. XPS analysis further revealed that the presence of MOF nanorods contributed to the formation of a less cross-linked polyamide structure, which increased the amount of free volume within the membrane and consequently improved its permeability.

(c) The improved hydrophilicity and porosity of the NH_2-Ce-BTC-500 membrane played a crucial role in reducing the impact of concentration polarization, including internal and external concentration polarization. By minimizing concentration polarization, the NH_2-Ce-BTC-500 membrane achieved a more efficient osmotic driving force, leading to improved performance in both FO and PRO processes. Water flux measurements conducted at different draw solution concentrations demonstrated that the NH_2-Ce-BTC-500 membrane exhibited a more linear response and higher water flux compared to the Ce-BTC-500 and pristine TFC membranes.

(d) The inclusion of MOF nanorods within the polyamide layer of the TFN membranes resulted in a reduction in specific solute flux (J_s/J_w). This was observed in both AL-FS and AL-DS configurations, suggesting a considerable improvement in water transport without sacrificing the membrane selectivity. Notably, the improvements were more pronounced in the NH_2-Ce-BTC-500 membrane compared to other membranes. In the analysis of PRO performance, the NH_2-Ce-BTC-500 membrane exhibited higher water flux (J_w) and lower specific solute flux (J_s/J_w) values compared to the Ce-BTC-500 and pristine TFC membranes. This indicates that the NH_2-Ce-BTC-500 membrane achieved a better balance between water transport and solute rejection, highlighting its enhanced selectivity and improved performance in the PRO process.

(e) The bench-scale improvements indicate a strong link to enhanced energy efficiency in larger-scale systems. Specifically, the NH_2-Ce-BTC-500 membrane boosts power density, potentially reducing the number of PRO modules needed in the Seawater Reverse Osmosis (SWRO)-PRO system, thereby cutting capital costs [95]. Achieving a power density of 6.9 W/m2 with this membrane in a full-scale PRO plant could significantly increase power generation from the same water volume, addressing key energy challenges in desalination and wastewater treatment. Moreover, this increase in power density could enhance the SWRO-PRO process's current performance, leading to energy savings and cost reductions. For instance, Japan's Mega-ton project's SWRO-PRO pilot plant anticipates a 10–30 % reduction in energy use [12,96]. Yip and Elimelech's [97] comparative analysis revealed that PRO could reach 54–56 % efficiency at 2.3–38 W/m2. Similarly, the Republic of Korea's Global MVP (Membrane distillation, Valuable source recovery and PRO) project reported approximately 20 % energy savings in the SWRO process by using the Toray PRO module [96].

4. Conclusion

MOF nanorods were found to improve the performance of TFN membranes for power generation in PRO. The NH_2-Ce-BTC-500 membrane outperformed the Ce-BTC-500 and pristine TFC membranes in key performance measures. Notably, the incorporation of amine-functionalized MOFs (NH_2-Ce-BTC) significantly increased the membrane's hydrophilicity, leading to a remarkable power density of 6.9 W/m^2 in the PRO process. This is in comparison to 6.0 W/m^2 for the Ce-BTC-500 membrane and 3.3 W/m^2 for the pristine TFC membrane, representing a substantial 109.1 % increase in power density compared to the TFC membrane. SEM and TEM images showed that MOFs increased surface roughness and porosity, creating additional water pathways, and increasing water flux to 31.0 LMH in PRO mode, 106 % higher than pristine TFC membranes. The increased water flux positively impacts power generation capacity and improves overall power generation efficiency by reducing downstream energy requirements. The findings of this study highlight the potential of the NH_2-Ce-BTC-500 membrane for enhancing PRO performance. Further exploration and optimization of MOF nanorod incorporation in TFN membranes hold promise for advancing osmotic power generation. Leveraging this energy-efficient and renewable power source could play a significant role in addressing the global energy crisis and fostering a sustainable future.

CRediT authorship contribution statement

Sadegh Aghapour Aktij: Conceptualization, Data curation, Formal analysis, Investigation, Methodology, Validation, Writing – original draft. **Mostafa Dadashi Firouzjaei:** Conceptualization, Data curation, Formal analysis, Funding acquisition, Investigation, Methodology, Project administration, Resources, Supervision, Validation, Writing – review & editing. **Seyyed Arash Haddadi:** . **Pooria Karami:** . **Amirhossein Taghipour:** Data curation, Formal analysis, Investigation.

Mehrasa Yassari: Data curation, Formal analysis, Investigation. **Asad Asad Asad:** . **Mohsen Pilevar:** Investigation. **Hesam Jafarian:** . **Mohammad Arjmand:** . **Mark Elliott:** . **Ahmad Rahimpour:** Conceptualization, Data curation, Formal analysis, Investigation, Methodology, Project administration, Supervision, Validation, Writing – review & editing. **João B.P. Soares:** . **Mohtada Sadrzadeh:** .

Declaration of competing interest

The authors declare that they have no known competing financial interests or personal relationships that could have appeared to influence the work reported in this paper.

Data availability

Data will be made available on request.

Acknowledgment

The financial support for this work by the Natural Science and Engineering Research Council of Canada (NSERC) and Canada's Oil Sands Innovation Alliance (COSIA) is gratefully acknowledged. Sadegh Aghapour Aktij acknowledges the financial support provided by the Killam Centre for Advanced Studies through the Izaak Walton Killam Memorial Scholarship, as well as the Alberta Innovates Graduate Student Scholarship (AIGSS), sponsored by Alberta Innovates of the Alberta government, Canada.

Appendix A. Supplementary data

Supplementary data to this article can be found online at https://doi.org/10.1016/j.cej.2023.148384.

References

[1] S. Uhlenbrook R. Connor The United Nations world water development report 2019 2019 leaving no one behind.
[2] M.D. Firouzjaei, S.K. Nemani, M. Sadrzadeh, E.K. Wujcik, M. Elliott, B. Anasori, Life cycle assessment of Ti3C2Tx MXene synthesis, Advanced Materials. N/a (2023) 2300422, https://doi.org/10.1002/adma.202300422.
[3] I.E. A, World Energy Outlook 2022, (2022).
[4] C. Le Quéré, R.B. Jackson, M.W. Jones, A.J.P. Smith, S. Abernethy, R.M. Andrew, A.J. De-Gol, D.R. Willis, Y. Shan, J.G. Canadell, Temporary reduction in daily global CO2 emissions during the COVID-19 forced confinement, Nat. Clim. Chang. 10 (2020) 647–653.
[5] G.P. Peters, R.M. Andrew, J.G. Canadell, P. Friedlingstein, R.B. Jackson, J. I. Korsbakken, C. Le Quéré, A. Peregon, Carbon dioxide emissions continue to grow amidst slowly emerging climate policies, Nat. Clim. Chang. 10 (2020) 3–6.
[6] E. Jones, M. Qadir, M.T.H. van Vliet, V. Smakhtin, S. Kang, The state of desalination and brine production: a global outlook, Sci. Total Environ. 657 (2019) 1343–1356.
[7] A.P. Straub, A. Deshmukh, M. Elimelech, Pressure-retarded osmosis for power generation from salinity gradients: is it viable? Energy Environ. Sci. 9 (2016) 31–48.
[8] B. Lee, L. Wang, Z. Wang, N.J. Cooper, M. Elimelech, Directing the research agenda on water and energy technologies with process and economic analysis, Energy Environ. Sci. (2023).
[9] M.D. Firouzjaei, S.F. Seyedpour, S.A. Aktij, M. Giagnorio, N. Bazrafshan, A. Mollahosseini, F. Samadi, S. Ahmadalipour, F.D. Firouzjaei, M.R. Esfahani, Recent advances in functionalized polymer membranes for biofouling control and mitigation in forward osmosis, J Memb Sci. 596 (2020) 117604.
[10] Z.M. Binger, A. Achilli, Forward osmosis and pressure retarded osmosis process modeling for integration with seawater reverse osmosis desalination, Desalination 491 (2020) 114583.
[11] H.-Q. Liang, W.-S. Hung, H.-H. Yu, C.-C. Hu, K.-R. Lee, J.-Y. Lai, Z.-K. Xu, Forward osmosis membranes with unprecedented water flux, J Memb Sci. 529 (2017) 47–54.
[12] S.J. Kwon, K. Park, D.Y. Kim, M. Zhan, S. Hong, J.-H. Lee, High-performance and durable pressure retarded osmosis membranes fabricated using hydrophilized polyethylene separators, J Memb Sci. 619 (2021) 118796.
[13] X. Tong, X. Wang, S. Liu, H. Gao, C. Xu, J. Crittenden, Y. Chen, A freestanding graphene oxide membrane for efficiently harvesting salinity gradient power, Carbon N y. 138 (2018) 410–418.
[14] P. Karami, S.A. Aktij, B. Khorshidi, M.D. Firouzjaei, A. Asad, M. Elliott, A. Rahimpour, J.B.P. Soares, M. Sadrzadeh, Nanodiamond-decorated thin film composite membranes with antifouling and antibacterial properties, Desalination 522 (2022) 115436.
[15] Y. Shi, M. Zhang, H. Zhang, F. Yang, C.Y. Tang, Y. Dong, Recent development of pressure retarded osmosis membranes for water and energy sustainability: a critical review, Water Res. 189 (2021) 116666.
[16] S.N. Rahman, H. Saleem, S.J. Zaidi, Progress in membranes for pressure retarded osmosis application, Desalination 549 (2023) 116347.
[17] M. Tawalbeh, A. Al-Othman, N. Abdelwahab, A.H. Alami, A.G. Olabi, Recent developments in pressure retarded osmosis for desalination and power generation, Renew. Sustain. Energy Rev. 138 (2021) 110492.
[18] R.R. Gonzales, Y. Yang, M.J. Park, T.-H. Bae, A. Abdel-Wahab, S. Phuntsho, H. K. Shon, Enhanced water permeability and osmotic power generation with sulfonate-functionalized porous polymer-incorporated thin film nanocomposite membranes, Desalination 496 (2020) 114756.
[19] W. Gai, D.L. Zhao, T.-S. Chung, Novel thin film composite hollow fiber membranes incorporated with carbon quantum dots for osmotic power generation, J Memb Sci. 551 (2018) 94–102.
[20] M.R. Esfahani, S.A. Aktij, Z. Dabaghian, M.D. Firouzjaei, A. Rahimpour, J. Eke, I. C. Escobar, M. Abolhassani, L.F. Greenlee, A.R. Esfahani, Nanocomposite membranes for water separation and purification: fabrication, modification, and applications, Sep. Purif. Technol. 213 (2019) 465–499.
[21] H. Choi, M. Son, H. Choi, Integrating seawater desalination and wastewater reclamation forward osmosis process using thin-film composite mixed matrix membrane with functionalized carbon nanotube blended polyethersulfone support layer, Chemosphere 185 (2017) 1181–1188.
[22] R. Rajakumaran, M. Kumar, R. Chetty, Morphological effect of ZnO nanostructures on desalination performance and antibacterial activity of thin-film nanocomposite (TFN) membrane, Desalination 495 (2020) 114673.
[23] N.A. Ahmad, P.S. Goh, K.C. Wong, A.K. Zulhairun, A.F. Ismail, Enhancing desalination performance of thin film composite membrane through layer by layer assembly of oppositely charged titania nanosheet, Desalination 476 (2020) 114167.
[24] M.D. Firouzjaei, M. Karimiziarani, H. Moradkhani, M. Elliott, B. Anasori, MXenes: The two-dimensional influencers, Mater Today Adv. 13 (2022) 100202.
[25] A.O. Rashed, A.M.K. Esawi, A.R. Ramadan, Novel polysulfone/carbon nanotube-polyamide thin film nanocomposite membranes with improved water flux for forward osmosis desalination, ACS Omega 5 (2020) 14427–14436.
[26] M.D. Firouzjaei, A.A. Shamsabadi, S.A. Aktij, S.F. Seyedpour, M. Sharifian Gh, A. Rahimpour, M.R. Esfahani, M. Ulbricht, M. Soroush, Exploiting synergetic effects of graphene oxide and a silver-based metal–organic framework to enhance antifouling and anti-biofouling properties of thin-film nanocomposite membranes, ACS Appl. Mater. Interfaces 10 (2018) 42967–42978.
[27] Y. Wen, Y. Chen, Z. Wu, M. Liu, Z. Wang, Thin-film nanocomposite membranes incorporated with water stable metal-organic framework CuBTTri for mitigating biofouling, J. Memb. Sci. 582 (2019) 289–297.
[28] R. Dai, X. Zhang, M. Liu, Z. Wu, Z. Wang, Porous metal organic framework CuBDC nanosheet incorporated thin-film nanocomposite membrane for high-performance forward osmosis, J. Memb. Sci. 573 (2019) 46–54.
[29] E. Zolghadr, M.D. Firouzjaei, S.A. Aktij, A. Aghaei, E.K. Wujcik, M. Sadrzadeh, A. Rahimpour, F.A. Afkhami, P. LeClair, M. Elliott, An ultrasonic-assisted rapid approach for sustainable fabrication of antibacterial and anti-biofouling membranes via metal-organic frameworks, Mater. Today Chem. 26 (2022) 101044.
[30] M. Pejman, M. Dadashi Firouzjaei, S. Aghapour Aktij, P. Das, E. Zolghadr, H. Jafarian, A. Arabi Shamsabadi, M. Elliott, M. Sadrzadeh, M. Sangermano, In situ Ag-MOF growth on pre-grafted zwitterions imparts outstanding antifouling properties to forward osmosis membranes, ACS Appl. Mater. Interfaces 12 (2020) 36287–36300.
[31] M. Pejman, M.D. Firouzjaei, S.A. Aktij, P. Das, E. Zolghadr, H. Jafarian, A. A. Shamsabadi, M. Elliott, M.R. Esfahani, M. Sangermano, Improved antifouling and antibacterial properties of forward osmosis membranes through surface modification with zwitterions and silver-based metal organic frameworks, J. Memb. Sci. 611 (2020) 118352.
[32] L. Pan, G. Liu, W. Shi, J. Shang, W.R. Leow, Y. Liu, Y. Jiang, S. Li, X. Chen, R.-W. Li, Mechano-regulated metal–organic framework nanofilm for ultrasensitive and anti-jamming strain sensing, Nat. Commun. 9 (2018) 1–10.
[33] M.D. Firouzjaei, A.A. Shamsabadi, M. Sharifian Gh, A. Rahimpour, M. Soroush, A novel nanocomposite with superior antibacterial activity: a silver-based metal organic framework embellished with graphene oxide, Adv. Mater. Interfaces 5 (2018) 1701365.
[34] X.-Y. Dong, Y. Si, J.-S. Yang, C. Zhang, Z. Han, P. Luo, Z.-Y. Wang, S.-Q. Zang, T.C. W. Mak, Ligand engineering to achieve enhanced ratiometric oxygen sensing in a silver cluster-based metal-organic framework, Nat. Commun. 11 (2020) 1–9.
[35] H. Jafarian, M.D. Firouzjaei, S.A. Aktij, A. Aghaei, M.P. Khomami, M. Elliott, E. K. Wujcik, M. Sadrzadeh, A. Rahimpour, Synthesis of heterogeneous metal organic Framework-Graphene oxide nanocomposite membranes for water treatment, Chem. Eng. J. 455 (2023) 140851.
[36] S.M. Nejad, S.F. Seyedpour, S.A. Aktij, M.D. Firouzjaei, M. Elliott, A. Tiraferri, M. Sadrzadeh, A. Rahimpour, Loose nanofiltration membranes functionalized with in situ-synthesized metal organic framework for water treatment, Mater. Today Chem. 24 (2022) 100909.
[37] M. Pejman, M.D. Firouzjaei, S.A. Aktij, E. Zolghadr, P. Das, M. Elliott, M. Sadrzadeh, M. Sangermano, A. Rahimpour, A. Tiraferri, Effective strategy for UV-mediated grafting of biocidal Ag-MOFs on polymeric membranes aimed at enhanced water ultrafiltration, Chem. Eng. J. 426 (2021) 130704.

[38] A. Zirehpour, A. Rahimpour, S. Khoshhal, M.D. Firouzjaei, A.A. Ghoreyshi, The impact of MOF feasibility to improve the desalination performance and antifouling properties of FO membranes, RSC Adv. 6 (2016) 70174–70185.
[39] S.F. Seyedpour, M. Dadashi Firouzjaei, A. Rahimpour, E. Zolghadr, A. Arabi Shamsabadi, P. Das, F. Akbari Afkhami, M. Sadrzadeh, A. Tiraferri, M. Elliott, Toward sustainable tackling of biofouling implications and improved performance of TFC FO membranes modified by Ag-MOF nanorods, ACS Appl. Mater. Interfaces 12 (2020) 38285–38298.
[40] D. Ma, S.B. Peh, G. Han, S.B. Chen, Thin-film nanocomposite (TFN) membranes incorporated with super-hydrophilic metal–organic framework (MOF) UiO-66: toward enhancement of water flux and salt rejection, ACS Appl. Mater. Interfaces 9 (2017) 7523–7534.
[41] X. Li, Y. Liu, J. Wang, J. Gascon, J. Li, B. Van der Bruggen, Metal–organic frameworks based membranes for liquid separation, Chem. Soc. Rev. 46 (2017) 7124–7144.
[42] A. Jeyaseelan, N. Viswanathan, Facile synthesis of tunable rare earth based metal organic frameworks for enhanced fluoride retention, J. Mol. Liq. 326 (2021) 115163.
[43] A. Jeyaseelan, I.A. Kumar, M. Naushad, N. Viswanathan, Fabrication of hydroxyapatite embedded cerium-organic frameworks for fluoride capture from water, J. Mol. Liq. 354 (2022) 118830.
[44] L. Zhao, X. Duan, M.R. Azhar, H. Sun, X. Fang, S. Wang, Selective adsorption of rare earth ions from aqueous solution on metal-organic framework HKUST-1, Chemical Engineering Journal Advances. 1 (2020) 100009.
[45] S.M. Prabhu, S. Imamura, K. Sasaki, Mono-, di-, and tricarboxylic acid facilitated lanthanum-based organic frameworks: insights into the structural stability and mechanistic approach for superior adsorption of arsenate from water, ACS Sustain. Chem. Eng. 7 (2019) 6917–6928.
[46] G. Chen, Z. Guo, W. Zhao, D. Gao, C. Li, C. Ye, G. Sun, Design of porous/hollow structured ceria by partial thermal decomposition of Ce-MOF and selective etching, ACS Appl. Mater. Interfaces 9 (2017) 39594–39601.
[47] A. Rahimpour, S.F. Seyedpour, S. Aghapour Aktij, M. Dadashi Firouzjaei, A. Zirehpour, A. Arabi Shamsabadi, S. Khoshhal Salestan, M. Jabbari, M. Soroush, Simultaneous improvement of antimicrobial, antifouling, and transport properties of forward osmosis membranes with immobilized highly-compatible polyrhodanine nanoparticles, Environ. Sci. Tech. 52 (2018) 5246–5258.
[48] Z. Haeri, M. Ramezanzadeh, B. Ramezanzadeh, Ce-TA MOF assembled GO nanosheets reinforced epoxy composite for superior thermo-mechanical properties, J. Taiwan Inst. Chem. Eng. 126 (2021) 313–323.
[49] S.A. Haddadi, S. Hu, S. Ghaderi, A. Ghanbari, M. Ahmadipour, S.-Y. Pung, S. Li, M. Feilizadeh, M. Arjmand, Amino-functionalized MXene nanosheets doped with Ce (III) as potent nanocontainers toward self-healing epoxy nanocomposite coating for corrosion protection of mild steel, ACS Appl. Mater. Interfaces 13 (2021) 42074–42093.
[50] J. He, Y. Xu, W. Wang, B. Hu, Z. Wang, X. Yang, Y. Wang, L. Yang, Ce (III) nanocomposites by partial thermal decomposition of Ce-MOF for effective phosphate adsorption in a wide pH range, Chem. Eng. J. 379 (2020) 122431.
[51] V.C. Anadebe, V.I. Chukwuike, S. Ramanathan, R.C. Barik, Cerium-based metal organic framework (Ce-MOF) as corrosion inhibitor for API 5L X65 steel in CO2-saturated brine solution: XPS, DFT/MD-simulation, and machine learning model prediction, Process Saf. Environ. Prot. 168 (2022) 499–512.
[52] M.D. Firouzjaei, M. Pejman, M.S. Gh, S.A. Aktij, E. Zolghadr, A. Rahimpour, M. Sadrzadeh, A.A. Shamsabadi, A. Tiraferri, M. Elliott, Functionalized polyamide membranes yield suppression of biofilm and planktonic bacteria while retaining flux and selectivity, Sep. Purif. Technol. 282 (2022) 119981.
[53] D.L. Pavia, G.M. Lampman, G.S. Kriz, J.A. Vyvyan, Introduction to spectroscopy, Cengage Learning (2014).
[54] Z. Zhou, B. Ling, I. Battiato, S.M. Husson, D.A. Ladner, Concentration polarization over reverse osmosis membranes with engineered surface features, J Memb Sci. 617 (2021) 118199.
[55] M.F. Gruber, C.J. Johnson, C.Y. Tang, M.h. Jensen, L. Yde, C. Hélix-Nielsen, Computational fluid dynamics simulations of flow and concentration polarization in forward osmosis membrane systems, J Memb Sci. 379 (2011) 488–495.
[56] Y. Oh, S. Lee, M. Elimelech, S. Lee, S. Hong, Effect of hydraulic pressure and membrane orientation on water flux and reverse solute flux in pressure assisted osmosis, J. Memb. Sci. 465 (2014) 159–166.
[57] A. Bogler, S. Lin, E. Bar-Zeev, Biofouling of membrane distillation, forward osmosis and pressure retarded osmosis: Principles, impacts and future directions, J. Memb. Sci. 542 (2017) 378–398.
[58] S.A. Aktij, A. Rahimpour, A. Figoli, Low content nano-polyrhodanine modified polysulfone membranes with superior properties and their performance for wastewater treatment, Environ. Sci. Nano. 4 (2017) 2043–2054.
[59] M. Zhang, X. You, K. Xiao, Z. Yin, J. Yuan, J. Zhao, C. Yang, R. Zhang, H. Wu, Z. Jiang, Modulating interfacial polymerization with phytate as aqueous-phase additive for highly-permselective nanofiltration membranes, J Memb Sci. 657 (2022) 120673.
[60] A. Asad, S.A. Aktij, P. Karami, D. Sameoto, M. Sadrzadeh, Micropatterned Thin-Film Composite Poly (piperazine-amide) Nanofiltration Membranes for Wastewater Treatment, ACS Appl Polym Mater. 3 (2021) 6653–6665.
[61] Y. Cao, Y. Wan, C. Chen, J. Luo, Preparation of acid-resistant nanofiltration membrane with dually charged separation layer for enhanced salts removal, Sep. Purif. Technol. 292 (2022) 120974.
[62] G. Kang, Y. Cao, Development of antifouling reverse osmosis membranes for water treatment: A review, Water Res. 46 (2012) 584–600.
[63] M. Zhao, S. Fu, H. Zhang, H. Huang, Y. Wei, Y. Zhang, Enhanced separation and antifouling performance of reverse osmosis membrane incorporated with carbon nanotubes functionalized by atom transfer radical polymerization, RSC Adv. 7 (2017) 46969–46979.
[64] L. Ma, Q. Bi, Y. Tang, C. Zhang, F. Qi, H. Zhang, Y. Gao, S. Xu, Fabrication of High-performance nanofiltration membrane using polydopamine and carbon nitride as the interlayer, Separations. 9 (2022) 180.
[65] S. Ma, X. Wu, L. Fan, Q. Wang, Y. Hu, Z. Xie, Effect of different draw solutions on concentration polarization in a forward osmosis process: theoretical modeling and experimental validation, Ind. Eng. Chem. Res. 62 (2023) 3672–3683.
[66] X. Wu, X. Zhang, H. Wang, Z. Xie, Smart utilisation of reverse solute diffusion in forward osmosis for water treatment: A mini review, Sci. Total Environ. 162430 (2023).
[67] D. Emadzadeh, W.J. Lau, T. Matsuura, N. Hilal, A.F. Ismail, The potential of thin film nanocomposite membrane in reducing organic fouling in forward osmosis process, Desalination 348 (2014) 82–88.
[68] B.L. Bonnett, E.D. Smith, M. De La Garza, M. Cai, J.V. Haag IV, J.M. Serrano, H. D. Cornell, B. Gibbons, S.M. Martin, A.J. Morris, PCN-222 metal–organic framework nanoparticles with tunable pore size for nanocomposite reverse osmosis membranes, ACS Appl. Mater. Interfaces 12 (2020) 15765–15773.
[69] X. Chen, W. Zhang, Y. Lin, Y. Cai, M. Qiu, Y. Fan, Preparation of high-flux γ-alumina nanofiltration membranes by using a modified sol–gel method, Microporous Mesoporous Mater. 214 (2015) 195–203.
[70] D. Hu, Z.-L. Xu, C. Chen, Polypiperazine-amide nanofiltration membrane containing silica nanoparticles prepared by interfacial polymerization, Desalination 301 (2012) 75–81.
[71] V. Vatanpour, S.S. Madaeni, L. Rajabi, S. Zinadini, A.A. Derakhshan, Boehmite nanoparticles as a new nanofiller for preparation of antifouling mixed matrix membranes, J Memb Sci. 401 (2012) 132–143.
[72] C.F. Wan, Y. Cui, W.X. Gai, Z.L. Cheng, T.-S. Chung, Nanostructured membranes for enhanced forward osmosis and pressure-retarded osmosis, in, Sustainable Nanoscale Engineering, Elsevier (2020) 373–394.
[73] C.Y. Tang, Q. She, W.C.L. Lay, R. Wang, A.G. Fane, Coupled effects of internal concentration polarization and fouling on flux behavior of forward osmosis membranes during humic acid filtration, J Memb Sci. 354 (2010) 123–133.
[74] J. Yin, E.-S. Kim, J. Yang, B. Deng, Fabrication of a novel thin-film nanocomposite (TFN) membrane containing MCM-41 silica nanoparticles (NPs) for water purification, J Memb Sci. 423 (2012) 238–246.
[75] H. Huang, X. Qu, X. Ji, X. Gao, L. Zhang, H. Chen, L. Hou, Acid and multivalent ion resistance of thin film nanocomposite RO membranes loaded with silicalite-1 nanozeolites, J Mater Chem A Mater. 1 (2013) 11343–11349.
[76] S. Xia, L. Yao, Y. Zhao, N. Li, Y. Zheng, Preparation of graphene oxide modified polyamide thin film composite membranes with improved hydrophilicity for natural organic matter removal, Chem. Eng. J. 280 (2015) 720–727.
[77] X. Liu, L.-X. Foo, Y. Li, J.-Y. Lee, B. Cao, C.Y. Tang, Fabrication and characterization of nanocomposite pressure retarded osmosis (PRO) membranes with excellent anti-biofouling property and enhanced water permeability, Desalination 389 (2016) 137–148.
[78] J. Benavente, M.I. Vázquez, Effect of age and chemical treatments on characteristic parameters for active and porous sublayers of polymeric composite membranes, J. Colloid Interface Sci. 273 (2004) 547–555.
[79] G.S. Lai, W.J. Lau, S.R. Gray, T. Matsuura, R.J. Gohari, M.N. Subramanian, S.O. Lai, C.S. Ong, A.F. Ismail, D. Emazadah, A practical approach to synthesize polyamide thin film nanocomposite (TFN) membranes with improved separation properties for water/wastewater treatment, J Mater Chem A Mater. 4 (2016) 4134–4144.
[80] S.F. Seyedpour, A. Rahimpour, A.A. Shamsabadi, M. Soroush, Improved performance and antifouling properties of thin-film composite polyamide membranes modified with nano-sized bactericidal graphene quantum dots for forward osmosis, Chem. Eng. Res. Des. 139 (2018) 321–334.
[81] L. Shen, S. Xiong, Y. Wang, Graphene oxide incorporated thin-film composite membranes for forward osmosis applications, Chem. Eng. Sci. 143 (2016) 194–205.
[82] S. Bano, A. Mahmood, S.-J. Kim, K.-H. Lee, Graphene oxide modified polyamide nanofiltration membrane with improved flux and antifouling properties, J Mater Chem A Mater. 3 (2015) 2065–2071.
[83] M.L. Lind, A.K. Ghosh, A. Jawor, X. Huang, W. Hou, Y. Yang, E.M.V. Hoek, Influence of zeolite crystal size on zeolite-polyamide thin film nanocomposite membranes, Langmuir 25 (2009) 10139–10145.
[84] R. Patel, W.S. Chi, S.H. Ahn, C.H. Park, H.-K. Lee, J.H. Kim, Synthesis of poly (vinyl chloride)-g-poly (3-sulfopropyl methacrylate) graft copolymers and their use in pressure retarded osmosis (PRO) membranes, Chem. Eng. J. 247 (2014) 1–8.
[85] S.E. Skilhagen, Osmotic power—a new, renewable energy source, Desalination, Water Treat. 15 (2010) 271–278.
[86] S. Chou, R. Wang, L. Shi, Q. She, C. Tang, A.G. Fane, Thin-film composite hollow fiber membranes for pressure retarded osmosis (PRO) process with high power density, J Memb Sci. 389 (2012) 25–33.
[87] Y. Chen, L. Setiawan, S. Chou, X. Hu, R. Wang, Identification of safe and stable operation conditions for pressure retarded osmosis with high performance hollow fiber membrane, J. Memb. Sci. 503 (2016) 90–100.
[88] G. Han, P. Wang, T.-S. Chung, Highly robust thin-film composite pressure retarded osmosis (PRO) hollow fiber membranes with high power densities for renewable salinity-gradient energy generation, Environ. Sci. Tech. 47 (2013) 8070–8077.
[89] J.H. Kim, S.J. Moon, S.H. Park, M. Cook, A.G. Livingston, Y.M. Lee, A robust thin film composite membrane incorporating thermally rearranged polymer support for organic solvent nanofiltration and pressure retarded osmosis, J Memb Sci. 550 (2018) 322–331.
[90] M. Tian, R. Wang, K. Goh, Y. Liao, A.G. Fane, Synthesis and characterization of high-performance novel thin film nanocomposite PRO membranes with tiered

nanofiber support reinforced by functionalized carbon nanotubes, J Memb Sci. 486 (2015) 151–160.
[91] S. Xu, F. Li, B. Su, M.Z. Hu, X. Gao, C. Gao, Novel graphene quantum dots (GQDs)-incorporated thin film composite (TFC) membranes for forward osmosis (FO) desalination, Desalination 451 (2019) 219–230.
[92] W.A. Phillip, J.S. Yong, M. Elimelech, Reverse draw solute permeation in forward osmosis: modeling and experiments, Environ. Sci. Tech. 44 (2010) 5170–5176.
[93] Y.C. Kim, M. Elimelech, Adverse impact of feed channel spacers on the performance of pressure retarded osmosis, Environ. Sci. Tech. 46 (2012) 4673–4681.
[94] N.-N. Bui, J.R. McCutcheon, Nanofiber supported thin-film composite membrane for pressure-retarded osmosis, Environ. Sci. Tech. 48 (2014) 4129–4136.
[95] S. Lee, J. Choi, Y.-G. Park, H. Shon, C.H. Ahn, S.-H. Kim, Hybrid desalination processes for beneficial use of reverse osmosis brine: Current status and future prospects, Desalination 454 (2019) 104–111.
[96] C. Lee, S.H. Chae, E. Yang, S. Kim, J.H. Kim, I.S. Kim, A comprehensive review of the feasibility of pressure retarded osmosis: Recent technological advances and industrial efforts towards commercialization, Desalination 491 (2020) 114501.
[97] N.Y. Yip, M. Elimelech, Comparison of energy efficiency and power density in pressure retarded osmosis and reverse electrodialysis, Environ. Sci. Tech. 48 (2014) 11002–11012.